Journal of Structural Geology 144 (2021) 104269

Contents lists available at ScienceDirect

Journal of Structural Geology

journal homepage: http://www.elsevier.com/locate/jsg

Evidence of hydrothermal fluid circulation driving elemental mass redistribution in an active fault zone

Matthew T. Dorsey [a,*,1], Thomas K. Rockwell [a], Gary H. Girty [a], Giles A. Ostermeijer [b], John Browning [b,2], Thomas M. Mitchell [b], John M. Fletcher [c]

[a] Department of Geological Sciences, San Diego State University, MC-1020, 5500 Campanile Dr., San Diego, CA, 92182-1020, USA
[b] Department of Earth Sciences, University College London, Gower Street, London, WC1E 6BT, UK
[c] Department de Geologia, Centro de Investigación Científica y de Educación Superior de Ensenada, Carretera Tijuana-Ensenada No. 3918, Zona Playitas, Ensenada, Baja California, 22860, Mexico

ARTICLE INFO

Keywords:
Hydrothermal alteration
Elemental mass redistribution
Fault zone architecture
Damage zone

ABSTRACT

Important fault zone processes can be discerned from the characterization of fracture damage and chemical transformations associated with active seismic sources. To characterize the 2010 M7.2 El Mayor-Cucapah rupture zone, continuous samples of fault core and 23 samples of damaged rock were collected perpendicular to strike of the Borrego fault. Samples were analyzed for clay mineralogy, bulk geochemistry, and bulk and grain density from which porosities and volumetric strains were derived. Prior to the Borrego fault forming, the tonalitic protolith, containing chlorite, epidote, and titanite, was subjected to temperatures of ~330–340 °C during deuteric alteration. Rocks within the damage zone are partially pulverized and contain abundant cataclastic seams. Porosity and volumetric strain peak in zones 1.5 m–10.5 m from the core. Within these zones, losses in Ca and P mass, increases in Mg and Na mass, along with the conservation of Fe and Si mass are consistent with oxidizing acidic conditions at < 200 °C. Gains in LOI are attributed to increases in clay content. The above data support a model of Mg- and Na-rich oxidizing fluid circulation within the damage zone of the Borrego fault.

1. Introduction

Within fault zones, granite permeability relies on the interconnection of pores or cracks and therefore is heavily dependent on fracturing resulting from fault slip events (Barton et al., 1995; Caine et al., 1996; Sibson, 1996; Zhang and Sanderson, 1996; Curewitz and Karson, 1997; Evans et al., 1997; Brown and Bruhn, 1998; Gudmundsson, 2000; Sheldon and Micklethwaite, 2007; Rockwell et al., 2009). Fault slip is accompanied, at least in part, by off-fault damage (Mitchell and Faulkner, 2009). Faulting typically produces a dramatic time dependent effect on the permeability structure of surrounding rocks due to fracturing and recovery during repeated earthquakes (Barton et al., 1995; Caine et al., 1996; Sibson, 1996; Zhang and Sanderson, 1996; Curewitz and Karson, 1997; Evans et al., 1997; Brown and Bruhn, 1998; Gudmundsson, 2000; Sheldon and Micklethwaite, 2007; Rockwell et al., 2009; Rempe et al., 2013). Faults can act as either barriers, conduits, or combined barrier-conduit systems to fluid flow. For example, Evans et al. (1997) recognized that well-developed damage zones can act as conduits for fluid flow, while both the fault core and wall rock are typically less permeable and act as barriers to flow.

Fluids play a vital role in the chemical and physical evolution of extensively fractured fault zones (Stierman, 1984; Bruhn et al., 1990, 1994; Parry et al., 1991; Hickman et al., 1995; Ishikawa et al., 2008; Morton et al., 2012). Fluids flowing through conduit-like damage zones have chemical compositions that reflect their source and migration pathways and carry the potential to cause mineralogical and chemical alteration of the protolith (Kerrich, 1986; Parry, 1998; Hagemann et al., 2007; Rossetti et al., 2010). At low temperatures (<200 °C), host rock geochemistry may have a dominant effect on fluid chemistry and the precipitation step can be rate controlling (Denny et al., 2019; Laubach et al., 2019). Significant geochemical and mineralogical anisotropies in fault zones are commonly produced by fluid-driven processes (Evans

* Corresponding author.
E-mail addresses: dorsey@tamu.edu (M.T. Dorsey), trockwell@sdsu.edu (T.K. Rockwell), ggirty@sdsu.edu (G.H. Girty), giles.ostermeijer.15@ucl.ac.uk (G.A. Ostermeijer), jbrowning@ing.puc.cl (J. Browning), tom.mitchell@ucl.ac.uk (T.M. Mitchell), jfletche@cicese.mx (J.M. Fletcher).
[1] Present address: Department of Geology and Geophysics, Center for Tectonophysics, Texas A&M University, College Station, Texas, USA.
[2] Present address: Department of Mining Engineering and Structural and Geotechnical Engineering, Pontificia Universidad Católica de Chile, Santiago, Chile.

https://doi.org/10.1016/j.jsg.2020.104269
Received 7 March 2020; Received in revised form 16 December 2020; Accepted 16 December 2020
Available online 9 February 2021

and Chester, 1995; Goddard and Evans, 1995).

This study was conducted on the well-exposed fault zone of the surface-rupturing 2010 El Mayor-Cucapah earthquake. Through a microstructural and geochemical approach, we focused on gaining an understanding of the physical and chemical processes operating in the Borrego fault zone, and how those processes have affected the various properties of the rocks making up the fault core and adjacent damage zone. Enhancement of permeability and subsequent fluid flow is interpreted to have driven mineralogical and chemical changes that we attempt to resolve in this study. Sampling techniques utilized in this study allow for a nearly continuous perspective of the microstructural, geochemical, and mineralogical development of key structural components in the fault zone.

1.1. Geologic setting

The Borrego fault is a right-lateral normal oblique-slip fault located in the Sierra Cucapah in northern Baja California, Mexico (Fig. 1). The Sierra Cucapah is a northwest trending mountain range that is geographically continuous with the Sierra El Mayor to the south. Both ranges comprise uplifted massifs of Mesozoic crystalline basement surrounded by rift valleys lying within the near sea level Gulf of California depression (Fig. 1A). The fault-controlled basins are filled with 2–5 km of syn-rift sedimentary deposits that include local fanglomerate, extra-regional deltaic deposits derived from the Colorado River, marine strata, and older Miocene volcanic rocks (Barnard, 1968; Kelm, 1972). Some of these units, e.g., the Pliocene Imperial and Pleistocene Palm Spring formations, crop out at various locations across the entire Salton Trough region (Dibblee Jr., 1954). In the Laguna Salada basin, adjacent to the active Laguna Salada fault, the Neogene sedimentary sequence is up to 4 km thick (Kelm, 1972; García-Abdeslem et al., 2001).

The basement of the Sierra Cucapah is composed largely of Mesozoic age plutons that have intruded an older sequence of pre-batholithic sillimanite-zone Paleozoic metasedimentary units, including gneiss, quartzite, amphibolite, and marble (Barnard, 1968; Axen and Fletcher, 1998). Most of the central and southern Sierra Cucapah comprises a compositionally zoned batholith with variably foliated, coarse-grained biotite tonalite surrounding a core of massive leucocratic granodiorite with some quartz monzodiorite and quartz diorite (Barnard, 1968). The mineralogy, geochemistry, texture, and compositional zoning of the batholith indicates that it is likely part of the La Posta-type suite, a group of trondhjemite-tonalite-granodiorite plutons named after the La Posta pluton near the Mexico-U.S. international border (Miller, 1935; Clinkenbeard, 1987; Clinkenbeard and Walawender, 1989; Walawender et al., 1990; Tulloch and Kimbrough, 2003). Barnard (1968) noted cross-cutting relationships that place a melanocratic phase as an intermediate pulse between the earlier La Puerta tonalite (~96 Ma U–Pb zircon) and the later Cucapah granodiorite (~93 Ma U–Pb zircon) (Moniz, 2008).

Relative motion between the Pacific and North American plates produced a transtensional tectonic regime extending from the Gulf of California northward through the Salton Trough. Faults in the Sierra Cucapah have diverse orientations and range in dip from 20° to 90° (Barnard, 1968; Axen and Fletcher 1998). This variation in geometry gives rise to extreme kinematic diversity (Fletcher et al., 2014, 2016). For example, during the 2010 Mw7.2 El Mayor-Cucapah earthquake, at least a portion of nearly every major fault in the Sierra Cucapah was activated. Incremental changes in fault orientation were systematically associated with incremental changes in the rake of slip during the El Mayor-Cucapah earthquake (Fletcher et al., 2014, 2016). In the study area, the Borrego fault is steeply dipping with a strike of 325°, which is consistent with a dextral to normal slip ratio of 2:3 (Fletcher et al., 2014, 2016).

The Borrego fault is one of several east dipping faults that terminate in the south at its intersection with the Laguna Salada fault. Slip on the east dipping faults is antithetic to the slip direction of the Laguna Salada fault, a dextral-normal oblique-slip fault that controls the west-facing escarpment of the Sierra Cucapah and its juxtaposition against the Laguna Salada rift basin. A narrow horst block (~750 m wide at the surface) of crystalline basement is developed between these two faults along the western flank of the Sierra Cucapah. Offset of a sharp vertical granodiorite-tonalite contact along the central part of the Borrego fault indicates total maximum dip slip of 4.3 km and a maximum vertical displacement of 3.5 km (Barnard, 1968), while the offset pinch-out of the melanocratic phase of the Cucapah granodiorite yields total dextral-normal oblique-slip of 6–8 km (Fletcher et al., 2020). Because transtensional shearing is now well documented to have occurred during the earliest phases of rifting in the proto-Gulf of California (Seiler et al., 2009), it is likely that the dextral-normal oblique-slip Borrego fault has been active since the onset of oblique rifting in this extensional province ca. 10–12 Ma (e.g., Mammerickx and Klitgord, 1982; Fletcher et al., 2007).

As evidenced by their association with paleoscarps, offset stream channels, trellised drainage systems, proximity to seismically recorded epicenters, and activation in large historic earthquakes, faults of the Sierra Cucapah and surrounding areas are unequivocally seismically active (Barnard, 1968; Hileman et al., 1973; Strand, 1980; Mueller and Rockwell, 1991; Fletcher et al., 2014, 2016; Rockwell et al., 2015). Based on paleoseismological evidence of the last four surface ruptures, the recurrence interval of large earthquakes (Mw7 or above) associated with the Borrego fault is estimated to be ~10,000 years (Hernandez Flores et al., 2013; Hernandez Flores, 2015).

2. Site characteristics

The study area is located in an arroyo on the western footwall block of a prominent uphill facing scarp formed during the 2010 Mw 7.2 El Mayor Cucapah earthquake (Fig. 2B). In a major flood event during the summer of 2013, the tectonically dammed arroyo was breached, which led to extensive erosion of the upthrown footwall, producing a well exposed scoured transect across the Borrego fault along the west-flowing arroyo floor (Fig. 2A). Post-earthquake erosion exposed an ~1.5 m thick fault core, and immediately adjacent to the core ~20 m of damaged rock (Ostermeijer et al., 2020) (Fig. 2C). The interval of damaged rock between ~20 m and ~40 m from the fault core is covered by alluvium. However, damaged rock is again exposed between ~40 m and ~52 m, and Ostermeijer et al. (2020) show that measured fracture densities display a power law decay reaching background levels ~85 m, thus defining the width of the footwall damage zone at this locality. Because the outer ~33 m of the damage zone is covered, we focused our work on the exposed portions lying within ~52 m of the fault core.

As shown in Fig. 2, meso-fracture density is most intense from 0 to ~10.5 m from the fault core, and is less intensely developed between ~13 m and ~20.3 m. Significantly though, pulverized rock occurs within a ~1.5 m thick band adjacent to the fault core (Fig. 2) (Ostermeijer et al., 2020), cataclasite textures are otherwise characteristic of these two zones while fault breccia is more common between ~40 m and ~52 m (Dorsey et al., 2017). In this paper, we refer to the above three parts of exposed damaged rock as zones 1 (0–~10.5 m), 2 (>~10.5 m–20.3 m) and 3 (~40 m–~52 m) (Fig. 2).

The NE dipping Borrego fault cuts the melanocratic phase of the Cucapah granodiorite, as well as parts of the La Puerta tonalite (Figs. 1B and 2A). Within the study area, the melanocratic phase of the Cucapah granodiorite is tonalitic, makes up the footwall block, and deformed remnants of it can be traced though the ~85 m thick damage zone and parts of the fault core (Fig. 2A).

3. Field and laboratory methods

A continuous 2-m long cross-section of fault core, weighing over 100 kg, was field-impregnated with epoxy, carefully extracted, and transported to the lab. Thin sections were produced from billets cut

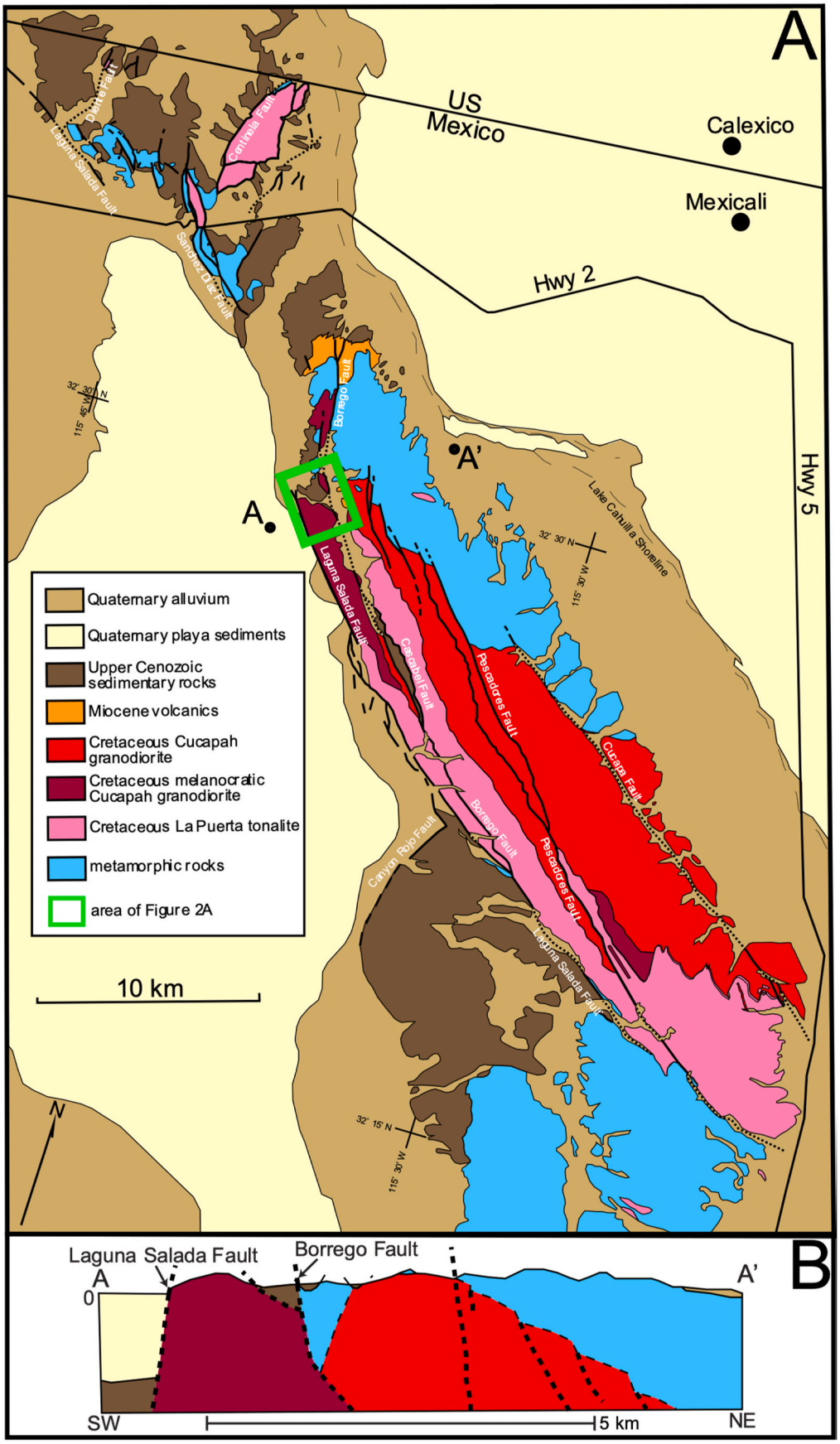

Fig. 1. (A) Regional geologic map of Sierra Cucapah modified from Barnard (1968). Line A to A′ is the approximate location of Fig. 1B. (B) Cross-section of the horst block of this study. Note, for sake of clarity, cross section is enlarged relative to scale of map but not vertically exaggerated. The dips of the Borrego and Laguna Salada faults are based on Fletcher et al. (2016).

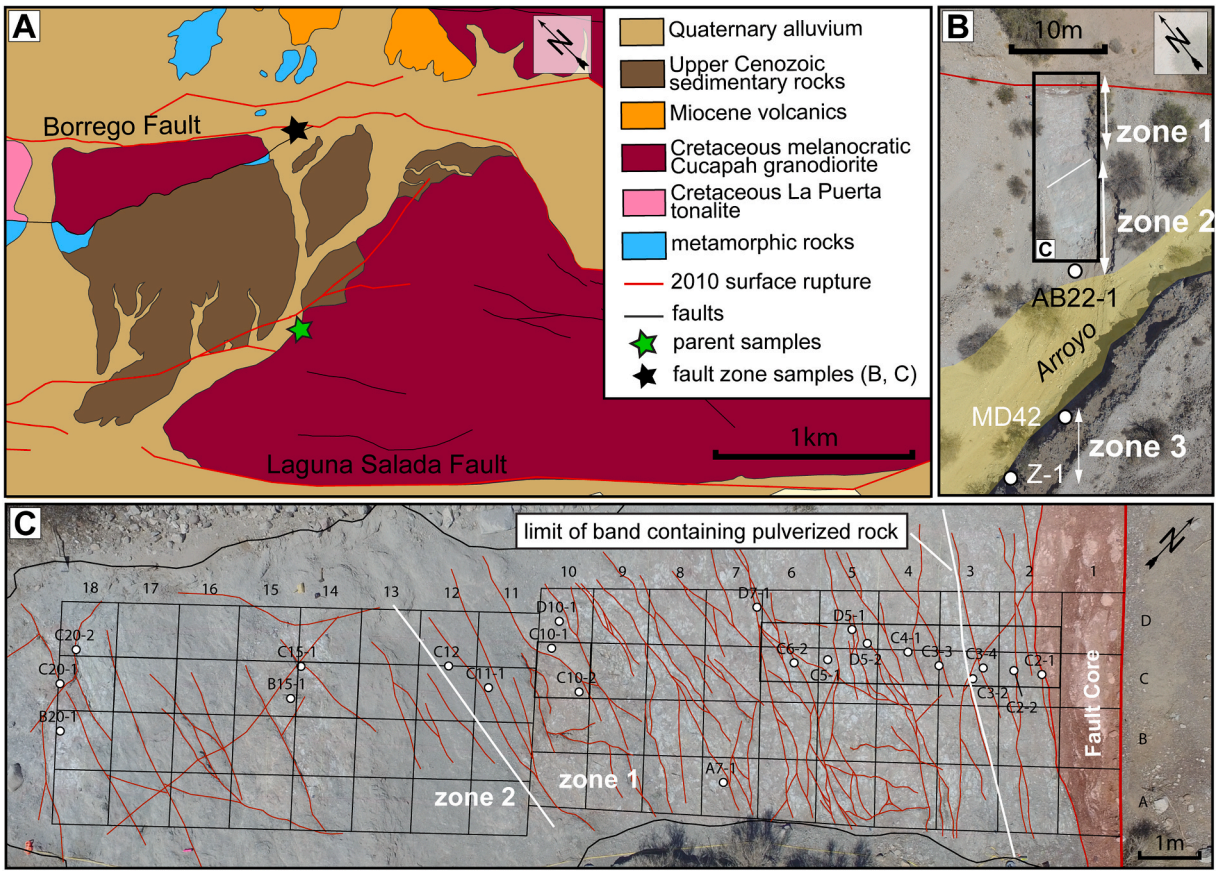

Fig. 2. (A) Map of area outlined by green box in Fig. 1A. (B) Aerial photograph including locations of 3 samples. Sample Z-2 was collected just off the map, southwest of Z-1, on the arroyo wall. The bold box is the area shown in Fig. 2C. (C) Outcrop map of study area showing fractures traced by Ostermeijer et al. (2020) along with additional sample locations. Gridding is 1 × 1 m spacing. (For interpretation of the references to color in this figure legend, the reader is referred to the Web version of this article.)

perpendicular to strike of the fault in both vertical and horizontal orientations across the entirety of the fault core.

Representative samples of the damage zone were collected for bulk geochemistry, beginning at the western edge of the fault core and extending westward for about 6 m into the footwall of the Borrego fault at approximately half-meter intervals (Fig. 2). Beyond 6 m, samples were collected approximately every meter up to 15 m from the fault core. Beyond 15 m from the fault core, three samples were collected between ~15 and 20 m and three additional samples were extracted between 40 and 55 m (Fig. 2). Alluvial cover prevented collection of samples between 20 and 40 m from the core. In order to preserve original textures, friable and poorly consolidated samples of the fault zone were cured with epoxy in the field. Following drying of epoxy and prior to removal from the outcrop, orientations were inscribed on each specimen. In addition, separate samples for chemical, density, and clay mineralogy were collected in the same sample locations (Fig. 2).

Thin sections of eight representative samples collected from zones 1 through 3 of the damage zone and one sample of the parent rock were prepared for petrological study. Each thin section was studied carefully, with a focus on identifying key mineralogical and textural characteristics of damaged and parent rock. However, of the initial collection, only five thin sections did not contain abundant clays, and were not water sensitive, and thus could be chemically stained to distinguish K-feldspar from plagioclase. These five samples were point counted using a 1.0 mm grid spacing. Depending upon the size of the slice of rock material adhering to the final stained thin section, between 300 and 400 points were counted in each sample at 100× magnifications using a mechanized Nikon Eclipse E400 POL microscope. Points falling under the cross hairs were counted and assigned to the following categories: quartz, plagioclase, K-feldspar, microcline, chlorite, epidote, white mica, sericite (i.e., microcrystalline aggregates of white mica altering from plagioclase), biotite, matrix, open void, calcite, opaques, and titanite (Table 1).

Table 1
Point-count results.

Sample	C2-1	MD42	Z-1	Z-2	INT2
zone	1	3	3	3	parent
distance (m)	0.1	41.0	46.0	52.0	~1000
Mineral	%	%	%	%	%
quartz	12.7	16.3	27.0	14.0	23.0
plagioclase	19.7	28.0	16.8	21.5	52.3
K-feldspar[a]	4.3	2.0	0.3	4.8	2.0
microcline[b]	0.0	0.0	0.0	0.0	1.3
chlorite	8.0	13.3	10.3	20.8	1.3
epidote	0.7	1.0	0.3	0.5	0.3
white mica[c]	0.3	0.0	0.0	0.0	0.3
sericite[d]	23.3	23.3	42.3	31.8	4.0
biotite	0.7	0.7	0.0	0.0	12.3
matrix	17.3	7.7	0.0	0.0	0.0
open void	11.7	3.3	1.8	1.8	1.3
calcite	1.0	3.0	1.0	3.0	0.0
opaques	0.3	1.3	0.5	0.5	0.3
titanite	0.0	0.0	0.0	1.5	1.3

[a] K-feldspar without gridiron twinning.
[b] Microcline based on gridiron twinning.
[c] Coarse flakes of white mica.
[d] Microcrystalline aggregates of white mica derived primarily from plagioclase alteration.

Following the initial point-count study, all eight thin sections representing damaged rock in zones 1 through 3 were recounted for grain or clast size, and then were classified using the scheme presented in Woodcock and Mort (2008). For this phase of the study, at 100× magnifications, 300 points were counted at a 1.0 mm grid spacing and were assigned to the following categories based on 2-D area and equivalent diameters: large (>2 mm), small (0.1–2 mm), matrix (<0.1 mm), open void, micrite, opaque cement, calcite cement (Appendix A).

Major and trace-element geochemical analyses were completed using standard X-ray fluorescence spectroscopy (XRF) at San Diego State University following the method of Girty et al. (2006). Results are presented in Table 2.

Bulk (ρ_b) and grain (ρ_g) densities of 13 samples were measured using a He-pycnometer at San Diego State University following methods described by Girty et al. (2008). Table 3 displays the results of this part of our study.

In order to gain some understanding of the precision of XRF chemical, and bulk and grain density data, we selected two large samples (~500 g/sample), one from 52 m (Z-2), and the other ~1 km (INT2) from the fault core (Fig. 2A). Z-2 is from zone 3, while INT2 is from the melanocratic tonalitic phase of the Cucapah granodiorite. Each sample was split into 4 sub-equal parts. In the case of INT2, each split was processed identically, and then was analyzed for all major elements. In contrast, in the case of Z-2, each part, following identical processing procedures, was evaluated for bulk and grain density.

Following analyses, coefficients of variation (CV) were calculated as the percent of the average of each oxide, bulk density, and grain density measurement, made up by the standard deviation (1σ), i.e., CV = 100* (1σ/average). For geochemical data, the CV reflects changes in chemical compositions over spatial scales of ~0.1–100+ m between samples, heterogeneities in mineral distributions at the scale of analyzed samples (~125 g/sample), accumulated errors during sample preparation, and machine error during analysis. In general, though the ranges in TiO_2, K_2O, and LOI result in CV of ~8%, ~12%, and ~17% respectively, geochemical data for all other elements are better than ~6% (Table 2). Such variation is attributed to alteration of the melanocratic tonalite prior to development of the Borrego fault (Dorsey et al., 2017). In contrast, ρ_b and ρ_g measurements are better than 1% (Table 3).

Clay-mineral analysis of the <2 μm fractions of eight samples was performed following conventional X-ray diffraction (XRD) analytical techniques described by Moore and Reynolds (1989). Samples were air-dried, ethylene glycol solvated, and heat saturated at 400 °C for 30 min and 550 °C for 30 min. Analyses were completed using a Philips

Table 3
Summary grain and bulk density measurements (g/cc).

Sample	grain density	bulk density	zone	distance (m)
C2-2	2.66	2.45	1	0.8
C3-3	2.72	2.29	1	1.8
D5-2	2.70	2.34	1	3.0
C6-2	2.70	2.35	1	4.1
C10-2	2.65	2.32	1	8.1
C11-1	2.72	2.31	1	9.8
C12	2.70	2.34	1	10.5
C15-1	2.72	2.40	2	13.1
AB22-1	2.69	2.53	2	20.3
MD42	2.73	2.59	3	41.0
Z-1	2.69	2.42	3	46.0
Z-2_1[a]	2.71	2.56	3	52.0
Z-2_2[a]	2.71	2.61	3	52.0
Z-2_3[a]	2.72	2.58	3	52.0
Z-2_4[a]	2.72	2.58	3	52.0
CV[b]	***0.21***	***0.80***		
INT2	2.71	2.645	parent[c]	1000

[a] Z-2 samples used for assessing precision.
[b] Coefficient of variation derived from Z-2 samples.
[c] Parent = melanocratic tonalite.

Table 2
Results from XRF analysis.

Sample	SiO_2	Al_2O_3	Fe_2O_3	CaO	MgO	K_2O	Na_2O	MnO	TiO_2	P2O5	LOI	zone	distance (m)
Wt. % = g/100g													
C2-1	65.3	15.8	3.26	2.36	1.84	2.72	4.69	0.072	0.516	0.148	3.04	1	0.1
C2-2	65.1	16.2	3.85	0.81	2.14	2.85	5.53	0.077	0.706	0.217	1.96	1	0.8
C3-4	62.1	16.8	3.74	2.30	2.48	3.02	5.20	0.087	0.529	0.140	3.39	1	1.3
C3-2	63.1	16.3	4.58	1.40	2.58	2.36	4.55	0.133	0.569	0.145	2.75	1	1.5
C3-3	66.1	16.3	3.05	0.94	1.72	3.40	5.32	0.064	0.456	0.132	1.88	1	1.8
C4-1	69.3	14.2	3.84	0.95	1.84	2.09	4.54	0.085	0.568	0.171	2.02	1	2.4
D5-2	69.0	14.9	3.40	1.87	1.50	1.84	4.47	0.062	0.624	0.169	2.08	1	3.0
C5-1	63.0	15.7	4.47	1.85	2.08	2.85	4.62	0.103	0.810	0.236	2.79	1	3.8
C6-2	66.8	15.6	3.48	0.97	2.23	1.74	5.54	0.068	0.734	0.209	2.03	1	4.1
D7-1	66.2	16.5	2.88	1.48	1.40	3.06	5.50	0.058	0.439	0.148	2.15	1	5.1
A7-1	66.3	16.4	2.95	1.18	1.67	3.21	5.10	0.066	0.489	0.154	2.20	1	5.9
C10-2	64.2	15.8	4.97	1.83	2.17	2.27	4.73	0.108	0.713	0.214	2.79	1	8.1
D10-1	66.8	14.7	3.36	1.96	1.54	2.42	4.98	0.081	0.576	0.162	2.55	1	8.9
C11-1	66.4	15.5	2.97	2.16	1.26	3.12	5.35	0.075	0.462	0.146	2.56	1	9.8
C12	65.9	17.4	2.61	0.58	1.22	1.72	7.93	0.055	0.554	0.162	1.21	1	10.5
C15-1	65.1	16.5	3.98	0.78	2.00	2.28	6.05	0.079	0.659	0.185	2.08	2	13.1
B15-1	63.9	16.1	3.14	2.97	1.53	3.11	4.76	0.091	0.500	0.152	3.39	2	13.9
C20-2	67.0	16.4	2.59	0.86	1.49	4.22	5.14	0.039	0.379	0.117	1.78	2	18.2
C20-1	63.8	16.0	3.05	2.78	1.60	2.28	6.17	0.079	0.680	0.205	3.35	2	18.9
AB22-1	64.6	16.6	3.56	1.34	1.68	2.74	5.26	0.065	0.680	0.210	2.13	2	20.3
MD42	60.0	17.0	5.56	2.62	2.70	3.63	5.05	0.096	0.799	0.231	2.90	3	41.0
Z-1F[a]	62.2	16.7	4.47	2.94	2.37	1.91	5.28	0.099	0.669	0.206	3.35	3	46.0
Z-2F[a]	56.8	17.0	6.00	5.01	3.21	2.16	3.76	0.122	0.933	0.276	4.41	3	52.0
INT2_1	66.5	16.3	3.91	3.78	1.36	1.94	4.14	0.063	0.665	0.231	0.87	Parent[b]	1000
INT2_2	67.5	16.4	3.46	3.35	1.29	2.41	3.98	0.062	0.568	0.204	1.23	Parent[b]	1000
INT2_3	66.3	16.5	3.87	3.70	1.41	1.86	4.30	0.065	0.673	0.230	1.00	Parent[b]	1000
INT2_4	66.6	16.5	3.78	3.55	1.40	2.22	4.07	0.068	0.636	0.224	1.24	Parent[b]	1000
CV[c]	***0.8***	***0.6***	***5.4***	***5.3***	***4.0***	***12***	***3.3***	***4.1***	***7.5***	***5.7***	***16.6***		

[a] Averages calculated using multiple splits.
[b] Parent = melanocratic tonalite.
[c] Coefficient of variation derived from INT2 samples.

X'Pert multipurpose diffractometer with copper Kα radiation (1.5405 Å), and 45 kV and 40 mA settings. Typical scans ranged from 3° to 32° 2θ.

4. Mathematical and statistical methods

4.1. Porosity and volumetric strain (ε)

Porosity (P) was determined from the following relationship:

$$P = 100^{*}\left(1 - \frac{\rho_b}{\rho_g}\right). \quad (1)$$

The results of these calculations are included in Appendix B and discussed further in following sections.

As discussed in Brimhall and Dietrich (1987) and Ague (1994), volumetric strain, ε, can be determined as follows:

$$\varepsilon = 100^{*}\left[\left(C_i^p / C_i^a\right)\left(\left(\rho_b^p / \rho_b^a\right) - 1\right]\right. . \quad (2)$$

In Eq. (2), C_i is the concentration of an immobile element, i.e., an element whose mass was conserved during fluid/rock alteration. Superscripts *p* and *a* identify parent and altered samples, respectively. We selected Al as a suitable immobile element as it meets the necessary statistical criteria described by Carrasco and Girty (2015), and also because it is commonly conserved during chlorite grade alteration (Parry and Downey, 1982; Eggleton and Banfield, 1985). Resulting data are provided in Appendix C and discussed in subsequent sections.

4.2. Estimating the uncertainties in changes in elemental mass

The transport function, τ, of Brimhall and Dietrich (1987) represents the percent change in an elements mass as a result of some metasomatic change. It is calculated as follows:

$$\tau = 100^{*}\left[\left(C_i^p / C_i^a\right)\left(C_m^a / C_m^p\right) - 1\right]. \quad (3)$$

In Eq. (3), C_i and the superscripts *p* and *a* are as defined for Eq. (2); C_m is the concentration of a likely mobile element. As noted above, Al was selected as the reference frame element. Utilizing Eq. (3), τ values were calculated for each sample (Appendix D).

Chemical compositions are constrained by both the range of each component and the constant sum constraint, i.e., $SiO_2 + Al_2O_3 + \ldots$ LOI = 1 or 100% (Aitchison, 1982, 1986, 1989). They are therefore not allowed to vary freely from -∞ to +∞, a necessary precondition for multivariate statistical analysis of compositional data (Pawlowsky-Glahn and Egozcue, 2006). However, the log-ratio transformation introduced by Woronow and Love (1990) circumvents this problem.

Using log ratios, Woronow and Love (1990) showed that

$$\ln(f_m) = \ln\left(C_m^a / C_i^a\right) - \ln\left(C_m^p / C_i^p\right), \quad (4)$$

where f_m is the multiplicative factor by which the mass of mobile element *m* changed, and all other symbols are as defined above. The significance of Eq. (4) is that once an element has been determined to be immobile, that element can be used to determine if the masses of other elements have been enriched ($f > 1$), depleted ($f < 1$), or experienced no change ($f = 1$) relative to its unaltered mass. The percentage change in mass of element *m* can be determined from

$$\Delta\%mass = 100\left(e^{(\ln(f_m))} - 1\right). \quad (5)$$

Eq. (5) represents a deterministic expression for calculating the percent change in elemental mass relative to an immobile component and yields results that are identical to the transport function, τ, of Brimhall and Dietrich (1987). In order to distinguish between percent change in elemental mass calculated from either Eq. (3) or Eq. (5), we will refer to the former as τ_{bd} and to the latter as τ_{wl}.

In practice, when following the method of Woronow and Love (1990), we average over a suite of samples, and thus need to assess the statistical significance of our results for each group of analyzed altered samples. To accomplish this task, we used the statistical algorithm outlined in Warren and Girty (1999) and shown in Table 4. Utilizing R, a language and environment for statistical computing (R Core Team, 2015), the mathematical and nine-step statistical procedures outlined in Table 4 were implemented in an R script, and the average percent change in elemental mass along with the associated 95% confidence interval for samples analyzed from zone 1 (0–10.5 m), zone 2 (>10.5–20.3 m), and zone 3 (40–52 m) were calculated. As noted in step 9 of Table 4, if the 95% confidence interval does not include 0, then the results are statistically significant, and a change in elemental mass likely occurred. Results derived from the R script are provided in Table 5 where statistically significant results are highlighted.

Another important consideration when estimating total uncertainty in element transport is the potential variability in parent materials. As described in Section 3, the coefficients of variation for the geochemical data are relatively low for most elements and high for only a few. This

Table 4
Algorithm used for assessing average changes in elemental mass and their statistical significance.

Steps	Procedure
1	For each sample, normalize all concentration values to the concentration of an immobile element.
2	Form the log-ratio of all chemical components in each sample by taking the logarithm of each value determined in Step 1 (e.g., $\ln(SiO_2/Al_2O_3)$, $\ln(TiO_2/Al_2O_3)$, $\ln(Fe_2O_3/Al_2O_3)$, etc.).
3	Calculate the average log-ratio value for each chemical component for both original and altered materials.
4	Substitute the resulting averages into equation (4), which is an expression of the difference in log-ratio means.
5	Use the F-test to test for equal or non-equal variances (Mendenhall and Beaver, 1994). If the given log-ratio for a specific element passes this test, then use the Student's *t*-test for equal variances to test H_o that there is no difference in log-ratio means. If, on the other hand, the given log-ratio does not pass the F-test, then use the Student's *t*-test for non-equal variances.
6	If the F-test indicates that the variances are probably unequal, then calculate the standard error for the difference in means, $s_{\bar{x}_2-\bar{x}_1}$, as follows: $s_{\bar{x}_2-\bar{x}_1} = \sqrt{\frac{s_1^2}{n_1}+\frac{s_2^2}{n_2}}$, where s_1^2 is the variance of the log-ratio values from the original material and s_2^2 is the variance of the log-ratio values for the altered material, and n_1 and n_2 are the number of samples used to characterize each sample (Mendenhall and Beaver, 1994). If, the F-test indicates that the variances are probably equal, then calculate the standard error for the difference in means using $s_{\bar{x}_2-\bar{x}_1} = \sqrt{\frac{s_p^2}{n_1}+\frac{s_p^2}{n_2}}$, where s_p^2 is a pooled estimator of the variance calculated as $s_p^2 = \frac{(n_1-1)s_1^2+(n_2-1)s_2^2}{(n_1-1)+(n_2-1)}$
7	Determine $t_{critical}$ for the predetermined confidence level (e.g., 95%) using as the degrees of freedom for equal variances $d.f. = n_1 + n_2 - 2$, and for unequal variances $d.f. = \left(\frac{s_1^2}{n_1}+\frac{s_2^2}{n_2}\right)^2 / \frac{\left(\frac{s_1^2}{n_1}\right)^2}{(n_1-1)} + \frac{\left(\frac{s_2^2}{n_2}\right)^2}{(n_2-1)}$, where all variables are as defined in previous steps.
8	The 95% confidence interval for the difference in log-ratio means is then $average[\ln(f_m)] \pm t_{\alpha/2}s_{\bar{x}_2-\bar{x}_1}$ where $t_{\alpha/2}$ represents the $t_{critical}$ value and the standard error of the difference in means is as calculated in Step 6. Under these constraints the maximum allowable $\ln(f_m)$ value is the average value of $\ln(f_m)$ plus the product of $t_{critical}$ and the standard error of the difference in means. In contrast, the minimum allowable value is the average value of $\ln(f_m)$ minus the value derived from multiplying $t_{critical}$ times the standard error of the difference in means.
9	Systematically substitute the maximum and minimum values calculated in Step 8 along with the calculated difference in means into equation (5) to form the 95% confidence interval about the average percentage change in elemental mass (Woronow and Love, 1990). If the interval bounded by the maximum and minimum values does not include zero, then reject H_o, and accept H_a that alteration has produced a change in elemental mass. On the other hand, if this interval includes zero, then there is no statistical evidence for rejecting H_o.

Table 5
Summary average τ_{wl} based on Al reference frame.

category	zone	Avg. % change	plus[a]	Minus[a]
$\tau_{wl\text{-}Si}$	1	2.0	8.7	8.0
	2	−2.1	2.4	2.3
	3	***−13.1***[b]	***6.2***	***5.8***
$\tau_{wl\text{-}Fe}$	1	−3.2	24.3	19.4
	2	−13.3	18.8	15.5
	3	***37.4***[b]	***29.9***	***24.5***
$\tau_{wl\text{-}Ca}$	1	***−59.8***[b]	***25.1***	***15.4***
	2	***−58.2***[b]	***49.2***	***22.6***
	3	−8.5	49.6	32.2
$\tau_{wl\text{-}Mg}$	1	***36.6***[b]	***40.3***	***31.1***
	2	***21.8***[b]	***17.9***	***15.6***
	3	***95.1***[b]	***40.3***	***33.4***
$\tau_{wl\text{-}K}$	1	24.5	34.7	27.1
	2	36.7	53.4	38.4
	3	14.3	65.5	41.6
$\tau_{wl\text{-}Na}$	1	***29.5***[b]	***17.4***	***15.4***
	2	***33.1***[b]	***19.9***	***17.3***
	3	9.6	30.0	23.5
$\tau_{wl\text{-}Mn}$	1	24.2	40.3	30.4
	2	6.0	53.4	35.5
	3	***58.4***[b]	***28.8***	***24.4***
$\tau_{wl\text{-}Ti}$	1	−6.3	23.8	19.0
	2	−10.3	33.8	24.5
	3	21.5	31.1	24.8
$\tau_{wl\text{-}P}$	1	***−21.8***[b]	***19.1***	***15.3***
	2	−23.0	26.9	19.9
	3	3.3	22.1	18.2
$\tau_{wl\text{-}LOI}$	1	***121.5***[b]	***77.3***	***57.3***
	2	***130.3***[b]	***117.0***	***77.6***
	3	***216.7***[b]	***139.9***	***97.0***

[a] 95% confidence interval.
[b] Statistically significant results bolded and italicized.

variability was attributed to pre-faulting alteration (Dorsey et al., 2017). Over the distance from the site where parent samples were collected to the fault zone (~1000 m), the parent rock appears uniform in texture and mineralogy. Furthermore, the mineralogy and textures of plutons of the La Posta series tend to be uniform over distances ≥2 km (Clinkenbeard, 1987; Clinkenbeard and Walawender, 1989). Notably, we used multiple samples of parent rock, but at a scale of cm. Thus, the parent samples are representative as the starting material prior to fault-related alteration.

5. Results

5.1. Thin section petrology

5.1.1. Parent rock

The parent rock in this study, identified by Barnard (1968) as the melanocratic phase of the Cucapah granodiorite, plots in the tonalite field of the IUGS QAP ternary diagram for plutonic rocks (Fig. 3F) (Table 1) (Le Maitre et al., 2005). In examined samples of tonalitic parent rock, hypidiomorphic-granular texture is well-preserved and sparse intragranular fracturing is evident (Fig. 3A). K-feldspar and quartz occur interstitially, whereas euhedral-subhedral plagioclase is locally sericitized. Plagioclase commonly displays albite, carlsbad, and polysynthetic twins while K-feldspar commonly exhibits the gridiron twin pattern characteristic of microcline. Platy to anhedral biotite is abundant and commonly becomes altered to chlorite + epidote ± titanite near contacts with plagioclase (Fig. 3C). Utilizing the Michel-Levy method, plagioclase is biaxial (+) oligoclase (~An_{12} - ~ An_{18}) (Kerr, 1959). Trace amounts of white mica, euhedral garnet, and opaque oxide minerals are also present. In comparison to fault zone rocks, the tonalitic parent rock is not heavily altered, and the local sericitization of plagioclase along with the chlorite-epidote-titanite assemblage replacing biotite likely reflects sub-solidus late-stage deuteric alteration (e.g., Kerr, 1959).

5.1.2. Fault core

The fault core is composed primarily of deformed and fragmented clasts of carbonate and lesser amounts of quartzofeldspathic and mica-rich clasts engulfed in an anastomosing foliated gouge and meso-cataclasite to ultracataclasite matrix. Clasts range in size from less than 1 mm to greater than 50 cm. Distinct textural and compositional domains exist within the fault core, some dominated by >90% matrix material, and others dominated by carbonate or quartzofeldspathic clasts >1 mm in size. Clasts are more common near the edges of the fault core and most of the larger clasts are carbonate. The main source of the smaller carbonate clasts are large centimeter to meter lenses of white and blue marble that are smeared along the strike of the fault (Fig. 4).

The fault core contains gouge-rich domains that differ in composition and color. Brownish gouge is typically richer in carbonate derived from marble smears, whereas, greenish gouge is rich in chlorite, and less commonly, quartzofeldspathic material (Fig. 4B). The portion of the fault core closest to the 2010 scarp is lighter brown in color and contains a significant component of sheared alluvium and other sedimentary rocks derived from the hanging wall (Fig. 4).

The restricted occurrence of carbonate in the fault core suggests that it may have been derived primarily from the hanging wall block, which contains marble and other types of metasedimentary rocks (Barnard, 1968). However, the same metasedimentary rocks are also likely to have made up portions of the footwall block at structural levels higher than are presently exposed at the surface. Carbonates were entrained, smeared, and fragmented in the fault core. Smearing of carbonate along the fault likely led to reduced permeability in the fault core (Færseth, 2006). In contrast, undeformed calcite and quartz-rich veins (<1 mm) are also present in the core and are probably derived from hydrothermal fluids that had infiltrated the core after the deformational fabrics had been acquired, but prior to its exhumation.

Near the contact between the fault core and footwall damage zone, tonalite clasts that vary in size from <1 mm up to ~10 cm are present and typically record the shearing and fragmentation of the footwall block, which is expected to occur prior to its incorporation into the fault core. Macroscopically, the appearance of tonalite clasts in the fault core marks the transition into the tonalitic footwall damage zone (Fig. 4). Microscopically, near the southwest edge of the fault core, a fossil principal slip surface juxtaposes clast populations dominated by quartzofeldspathic material and those dominated by carbonate material (Fig. 4C). Another discrete slip surface that was activated in the 2010 rupture is observed to truncate older fabrics and cut out sections of the fault core producing along-strike heterogeneities in core thickness. In fact, to the southeast of the river-cut platform, the vertical scarp-forming fault completely cuts out the long-lived undulating fault core. Therefore, these discrete slip surfaces within the core must strongly affect the distribution of strength heterogeneities along the fault.

5.1.3. Damage zone

As noted earlier, we have subdivided the exposed portion of damaged rock into zones 1 (0–~10.5 m), 2 (>~10.5 m–20.3 m) and 3 (~40 m–~52 m) (Fig. 2). Rocks within zones 1 and 2 display grain sizes characteristic of the cataclasite series (Fig. 5D) (Woodcock and Mort, 2008). Additionally, two of the innermost point-counted samples (C2-1 and C2-2) in zone 1 were collected from the ~1.5 m thick band adjacent to the fault core that includes pulverized rock (Fig. 2) (Ostermeijer et al., 2020). Much of the grain size reduction in this innermost ~1.5 m thick portion of zone 1 is due to extensional grain fragmentation and partial pulverization while cataclasite textures are found primarily in shear bands. The three samples collected furthest from the fault core in zone 3 are notably coarser grained than samples collected closer to the fault in zones 1 and 2. Based on grain size, two are classified as breccia while the third is a protocataclasite (Fig. 5D) (Woodcock and Mort, 2008).

Though there are marked differences in textures and fracture density, mineralogical features of samples from zones 1 through 3 are similar. Hence, to avoid redundancy, we here focus on the differences

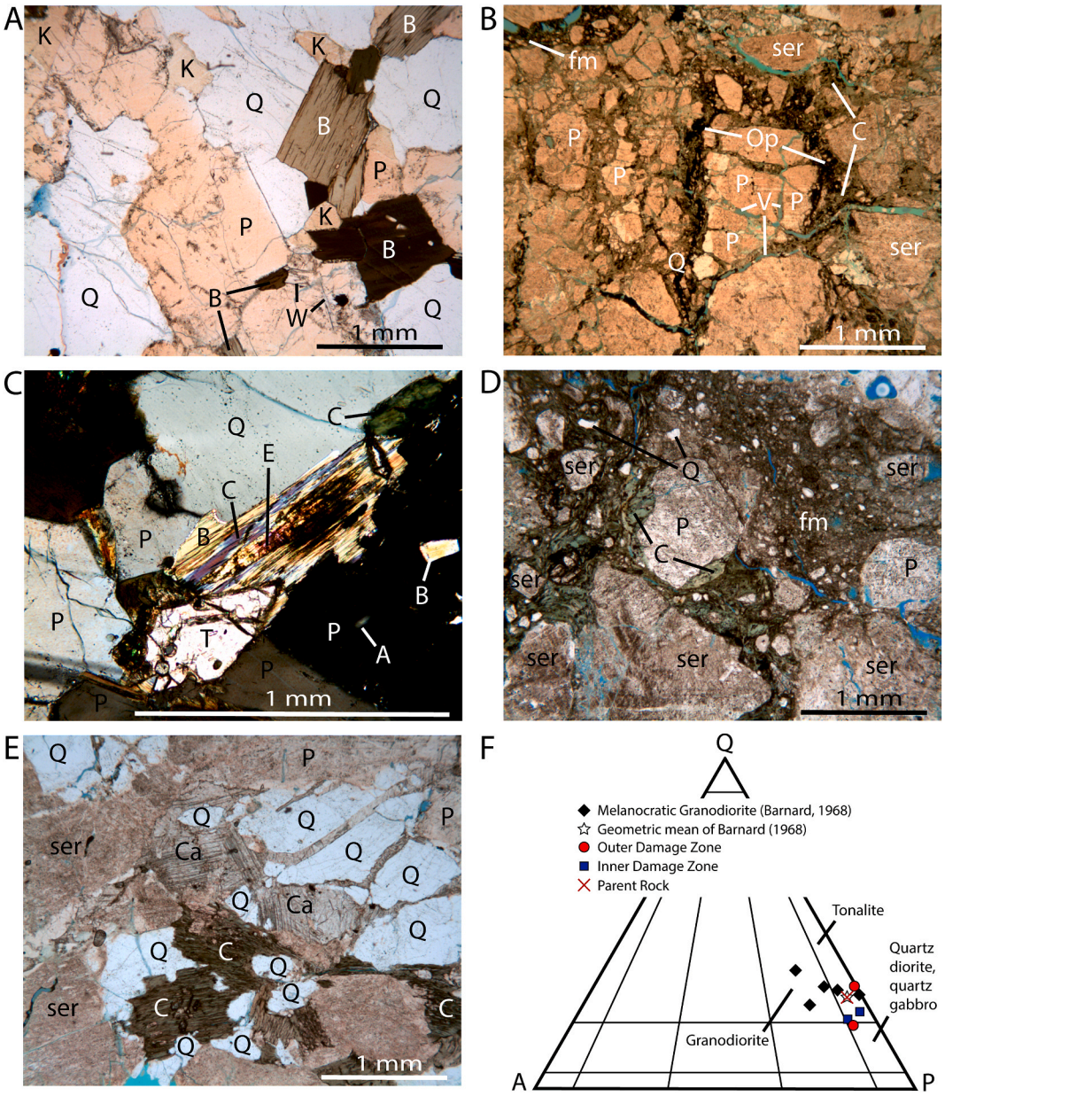

Fig. 3. Photomicrographs. (A) Parent rock (INT2) showing representative relic igneous texture with unaltered biotite. (B) Sample MD42 displaying a breccia to protocataclasite texture. (C) Representative alteration assemblage of parent rock. Plagioclase and biotite are partially altered to chlorite, epidote, and titanite. (D) Representative mesocataclasite texture of zone 1 (C2-2). (E) Representative chaotic breccia texture of zone 3 (Z-1). In addition, this photomicrograph shows sealing of fractures by calcite. Note, in this image, all biotite has been replaced by chlorite. (F) Samples from this study plotted on IUGS QAP ternary diagram for plutonic rocks (Le Maitre et al., 2005). The geometric mean of point counts by Barnard (1968) derived from same unit is similar to that derived from this study. A = apatite; B = biotite; C = chlorite; Ca = calcite; E = epidote; fm = fine-grained matrix; K = K-feldspar; Op = opaque cement; P = plagioclase; Q = quartz; ser = sericite; T = titanite; V = void; W = white mica.

between these three zones. Protocataclasites and mesocataclasites occur throughout zone 1, but only protocataclasite was identified in zone 2 (Fig. 5D). In contrast, samples from zone 3 are notably coarser grained and vary from protocataclasite to chaotic breccia (Fig. 5D). In zone 1, large clasts are less abundant (0–2%), and matrix (42–54%) is more prevalent than in zones 2 and 3 where large clasts make up 14–47% and matrix makes up 5–37% (Fig. 3B). In contrast, the percentage of small clasts varies across all three zones. Moreover, rocks in zone 1 show evidence of significant comminution, particularly in sheared bands that become more pervasive towards the fault core. These rocks are dominated by monomineralic clasts with less abundant polymineralic clasts that preserve relic tonalitic textures.

Within zone 3, the grain/clast size transitions from a protocataclasite to a heavily altered and damaged breccia. Point counted samples from zone 3 reveal grain/clast sizes characteristic of chaotic breccia (Fig. 5D) (Woodcock and Mort, 2008). However, clasts/grains in these samples show little to no rotation and therefore fit the textural description of a crackle breccia (Woodcock and Mort, 2008). Coarser grained mosaic and crackle breccias with ~5% matrix are also present (Fig. 3E). Protocataclasite to mesocataclasite seams cut the breccia fabric and are primarily composed of comminuted plagioclase and quartz grains with smaller amounts of fragmented chlorite, calcite, and clays. The bounds of such seams are defined by an abrupt reduction in fracture density and the lack of matrix.

The mineral content of samples across all three exposed zones of damaged rock show little variation as revealed from point counting

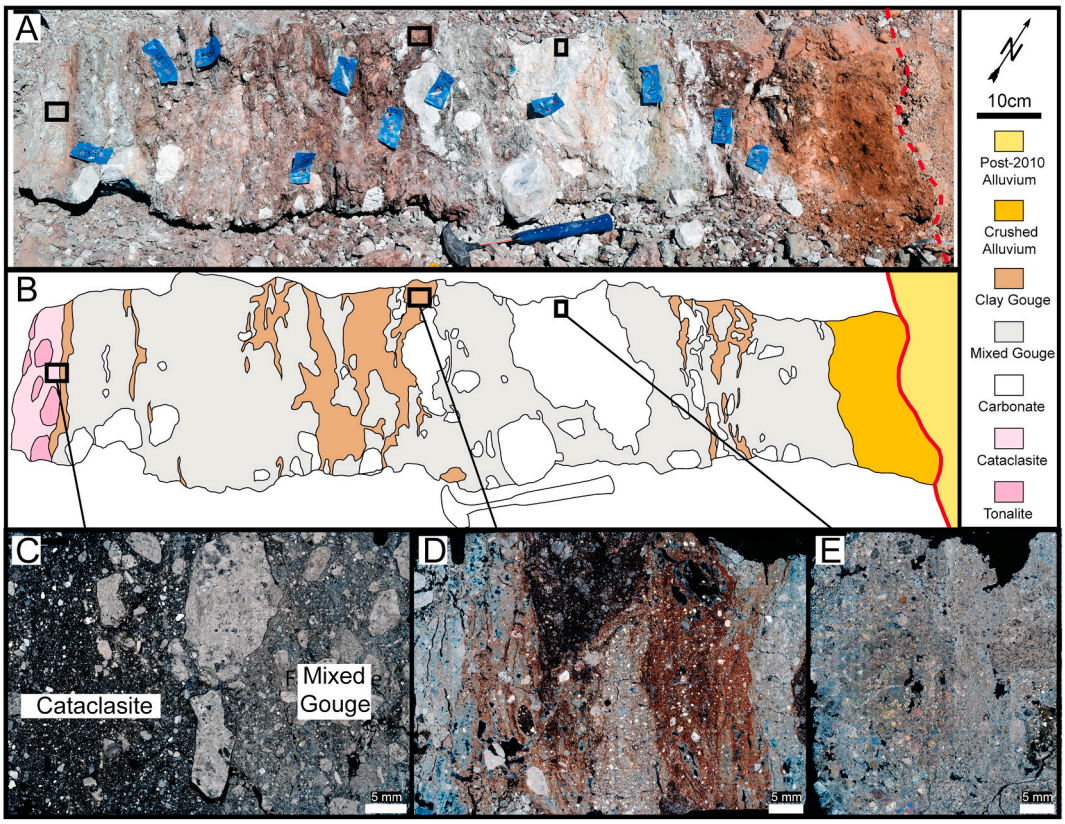

Fig. 4. (A) Continuous fault core sample collected for this study. (B) Schematic representation of the fault core sample from (A). (C) Photomicrograph of a transition in the composition of the fault core under cross-polarized light. The right is marked by a lighter overall color and high carbonate content while the left side is richer in quartz, feldspar, and mica. Between the differing compositions is likely the pre-2010 principal slip surface. (D) Photomicrograph of foliated gouge under cross-polarized light. (E) Cross-polarized photomicrograph of fragmented carbonates, part of the white smear observed in outcrop. (For interpretation of the references to color in this figure legend, the reader is referred to the Web version of this article.)

samples that were stained to distinguish plagioclase from K-feldspar (Table 1). Throughout the damage zone, the primary tonalitic mineral assemblage is significantly modified by sericitization of plagioclase and chloritization of biotite. Damage zone rocks also are typically more rich in clays as compared to host rock samples. Some damage zone rocks contain an opaque oxide interstitial cement associated with cataclasite seams, which is not observed in the protolith. Calcite is present primarily as infill in highly fractured rock, and to a lesser extent, as an alteration product of plagioclase. Calcite displays abundant deformation twins but becomes more fibrous in cataclasite dominated domains. In some cases, undeformed calcite surrounds broken quartz fragments, and therefore reflects sealing following cataclasis.

The abundance of secondary minerals such as chlorite and sericite are correlated with an increase in intragranular cracks and calcite veins. Some calcite veins are crosscut and comminuted by mesocataclasite to ultracataclasite seams suggesting that they formed during progressive cataclasis.

Textural evidence for albitization of oligoclase is relatively common throughout the exposed portions of the damage zone. For example, in specimens chemically stained to distinguish plagioclase from K-feldspar, where calcite veins transect fragmented and sericitized oligoclase, unstained haloes of plagioclase lacking sericitization are evident (Fig. 5A). The unstained haloes lack the An component of plagioclase and are likely albite ($Ab_{90\text{-}100}An_{10\text{-}0}$), while more lightly stained portions are probably An-poor oligoclase (Bailey, 1960) (Fig. 5A). Similar rinds or haloes of unsericitized low-An oligoclase to albite have developed locally around sericitized plagioclase fragments (Fig. 5B and C).

5.2. Clay mineralogy

Fig. 6 shows clay mineralogy data from the <2 μm fraction of selected samples. Throughout the damage zone and parent rock, illite and chlorite are evident in all analyzed samples (Moore and Reynolds, 1989). Kaolinite is likely present in all or most samples but cannot be easily differentiated from chlorite due to the overlapping of the 7.16 Å kaolinite and 7.10 Å chlorite peaks (Fig. 6). For example, Moore and Reynolds (1989) note that the 7.10 Å, 4.74 Å, and 3.55 Å peaks of chlorite will be weakened, *but not eliminated*, when heat treated at 550 °C for 1 h. Most samples display these characteristics, but in some, the 7.10 Å and 4.74 Å peaks are completely destroyed after heat saturation treatment at 550 °C (Fig. 6). Based on this behavior, we infer that kaolinite is likely present in these samples.

In addition to the above clays, mixed-layer kaolinite/smectite also is likely present in samples from zone 1 and may occur in limited amounts in specimens from zone 3. This observation is based primarily on the presence of a ~7.7 Å peak in the glycolated sample and its shift to ~8.0 Å upon 400 °C heat saturation treatment (Fig. 6). Based on Δ° 2θ data in Table 8.6 in Moore and Reynolds (1989), kaolinite makes up 70–80% of the mixed-layer kaolinite/smectite.

Small quantities of discrete smectite are present in the parent rock and in zone 1 but is not present in zone 3 (Fig. 6). Discrete smectite is indicated by the expansion of the ~15.0 Å peak to 16.9 Å, and the appearance of an 8.46 Å peak following ethylene glycol solvation (Fig. 6) (Moore and Reynolds, 1989).

Hydroxy-interlayered vermiculite (HIV) is present in zone 1 but does not appear to be present in the zone 3 samples or in the parent rock. This interpretation is based on the collapse of 14 Å peaks to ~12 Å after heat saturation treatment at 400 °C (Fig. 6). The 12 Å peaks subsequently

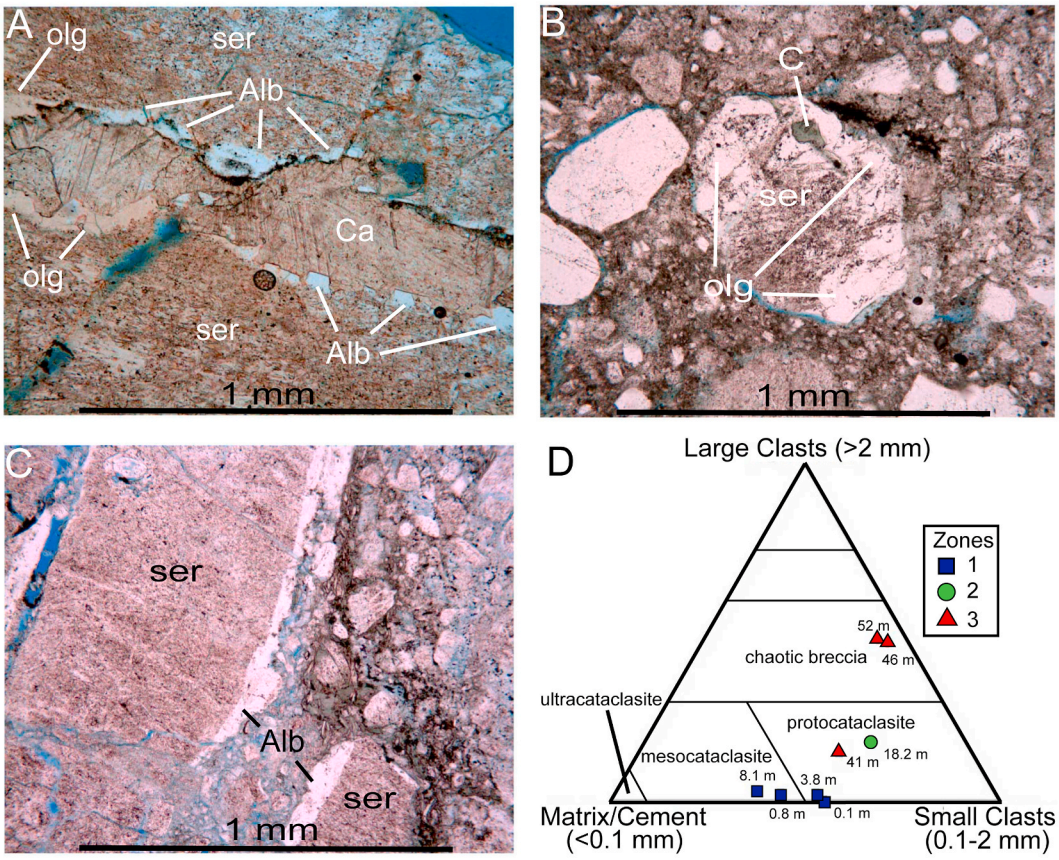

Fig. 5. Photomicrographs. Abbreviations are the same as Fig. 3 (A) Calcite vein in sample Z-1 showing an alteration halo of low An oligoclase to pure albite. The low An oligoclase has not been sericitized and the albite remains unstained. (B) Plagioclase fragment in sample C5-1 displaying low An oligoclase to albite rim with sericitized core. (C) Plagioclase clast and a broken-off clast displaying unaltered albite rims with sericitized cores. Alb = albite; olg = low An oligoclase. (D) Samples from zones 1 through 3 plotted on the fault rock classification scheme of Woodcock and Mort (2008). Point-count data are provided in Appendix A. Distances from fault core are written next to points.

collapse further to ~11.8 Å after heat treatment at 550 °C (Harris et al., 1992; Righi et al., 1993; Purcell et al., 2015).

Mixed-layer illite/smectite, with varying proportions of illite, is present in zones 1 and 3 (Fig. 6). It also is present in samples of the parent tonalitic material (Fig. 6). Mixed-layer illite/smectite is identified in samples by the appearance of an ~5.1 Å peak following ethylene glycol solvation (Moore and Reynolds, 1989). Percent illite in mixed-layer illite/smectite, estimated from Table 8.3in Moore and Reynolds (1989), is typically 80–90%.

The remainder of the <2 μm fractions analyzed during this study is made up of primarily plagioclase, quartz, and microcline. The presence of these silicate minerals in the <2 μm fraction derived from the damage zone is interpreted to be due primarily to cataclasis or tensile grain shattering. In contrast, their presence in the parent tonalite is a relic of the separation process, which involved crushing using a mechanized rock chipper.

In summary, the results of our XRD work, supplemented by thin section observations, indicate that biotite to various degrees has been altered to chlorite and lesser amounts of smectite in the parental tonalite. In the damage zone, chlorite has been broken down further to HIV (Righi et al., 1993). Thin section study of samples from zones 1, 2, and 3 suggests that they contain an order of magnitude higher proportion of chlorite than does the parental tonalite (Table 1). The sericitic alteration of plagioclase observed in thin sections of the parental tonalite is likely composed primarily of illite, smectite, and kaolinite. In the damage zone, these assemblages are more intensely developed. Mixed-layer kaolinite/smectite, and lesser amounts of illite/smectite are prominent in zone 1 but appear to be less well developed in zone 3 (Fig. 6). In summary, the greater alteration displayed by samples collected from throughout the damage zone likely reflects an increase in fluid flow through these zones in comparison to the parental tonalite.

5.3. Porosity and volumetric strain

The background porosity of the tonalitic parent rocks, based on bulk and grain density values measured on one sample, is 2% ± 1.6%. Within the damage zone, porosity generally increases toward the fault core, rising from ~5% in zone 3, to 6%–11% in zone 2, to 13%–16% within zone 1, before falling off to ~8% within the band containing pulverized rock 0.8 m from the fault core (Fig. 7). The small data set along with the absence of analyzed samples from the ~20 m–~40 m covered section inhibits efforts to obtain a best-fit solution to data displayed in Fig. 7. However, if the one sample from the band containing pulverized rock is excluded, then an exponential best-fit curve appears to be a reasonable fit ($y = 14.613e^{-0.019x}$; $R^2 = 0.648$). The resulting best-fit curve reaches tonalitic background porosities at ~68 m (Fig. 7). Matrix fraction (Appendix A) also follows a negative exponential form with distance from the fault, consistent with decreasing microfracture intensity.

Volumetric strain data (ε) are plotted against distance from the fault core in Fig. 7. Relative to tonalite outside the damage zone, ε increases from −1% - 8% in zone 3, to 3%–12% in zone 2. In contrast, within zone 1, ε values vary between ~16% and ~25% within 9.8 m–1.8 m from the fault core. This band of relatively high ε values are bounded by lower values of ~7% and ~9% at 10.5 m and 0.8 m respectively from the fault core. The latter value is from the band containing pulverized rock. If it is eliminated from consideration, then the logarithmic best-fit curve (y =

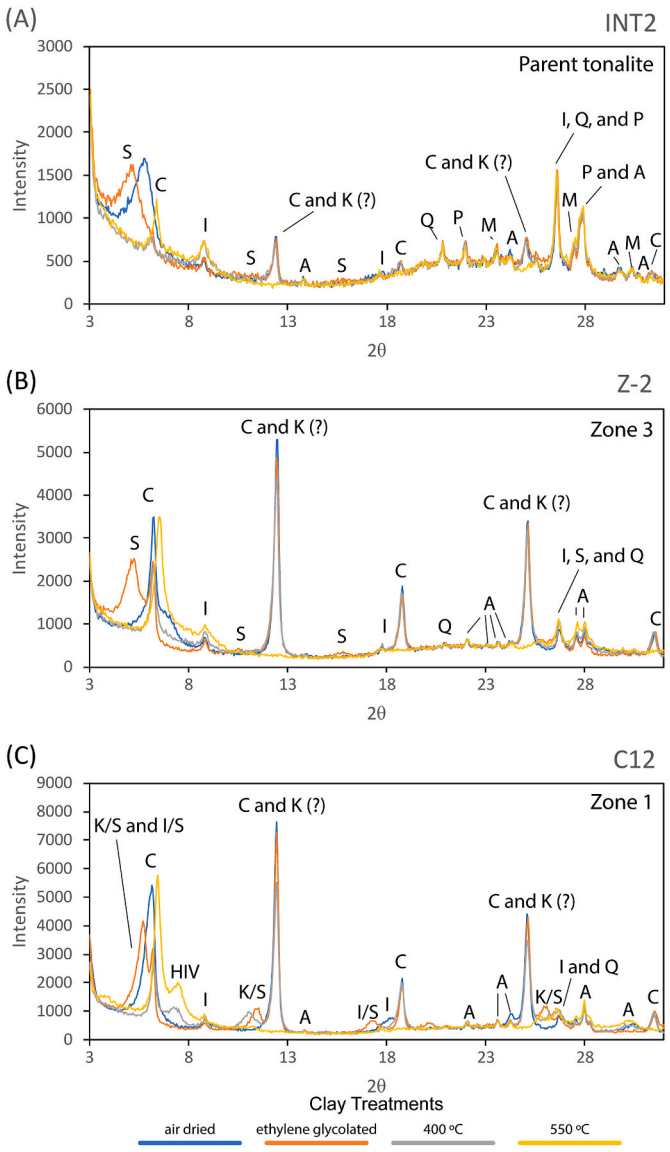

Fig. 6. X-ray diffractograms of the <2 μm fraction. (A) parent tonalite, (B) zone 3, (C) zone 1. The y-axis varies from plot to plot due to the variability in amounts of clay in each sample and quality of clay slide. Key mineral peaks (Å) are as follows. S = smectite (17.1–17.5, 8.5, 5.6, 3.4 glycolated). K/S = kaolinite/smectite (15.4, 7.7, 3.4 glycolated; 8.0 400 °C). I/S = illite/smectite (15.4, 5.1, glycolated). C = chlorite (14.1–14.2, 7.1, 4.7, 3.6, 2.8). HIV = hydroxy-interlayered vermiculite (11.9 400 °C; 11.7 550 °C). I = illite (10.0–10.1, 4.9–5.0, 3.4). K = kaolinite (7.1, 3.6). A = albite (6.4, 4.0, 3.8, 3.7, 3.2, 3.0, 2.9). Q = quartz (4.2–4.3, 3.4). P = plagioclase (4.0, 3.4, 3.2). M = microcline (3.4, 3.2, 3.0).

$-6.557\ln(x) + 27.576$; $R^2 = 0.665$) displayed in Fig. 7 appears to be an adequate fit. Logarithmic best-fit was used because standard best-fit exponential techniques do not allow negative values. Notably, the resulting curve reaches 0 volumetric strains at ~68 m (Fig. 7). Thus, results from porosity and volumetric strain measurements yield identical results that suggest a damage zone width of ~68 m. These estimates are less than the 85 m determined from the more robust set of fracture data in Ostermeijer et al. (2020). However, they may imply that porosity and volumetric strains decline more rapidly to background levels than do meso-fracture densities, and thus yield smaller estimates of damage zone width.

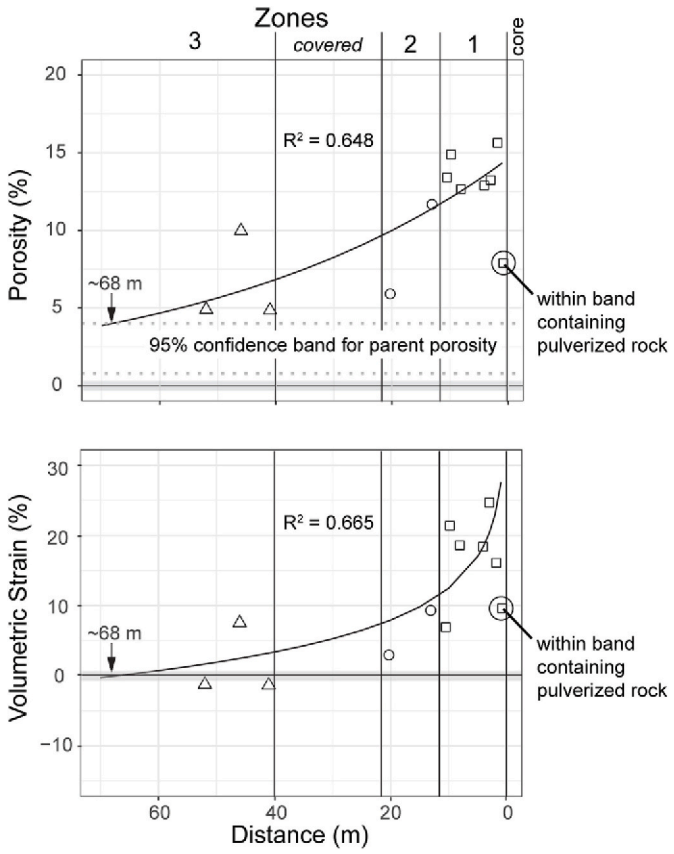

Fig. 7. Porosity and volumetric strain (ε) plotted against distance from fault core. Data are listed in Appendices B and C, respectively. Arrow at ~68 m distance from fault core is the indicated width of the damage zone based on the best-fit curves.

5.4. Geochemistry

In this study, the goal of geochemical analyses was to quantify changes in elemental mass resulting from damage and alteration in an active fault zone (Table 5). Therefore, elemental mass redistribution, in comparison to the tonalitic parent rock, is the primary focus of this section. To assess the spatial pattern of elemental mass redistribution in zones 1 through 3, τ_{bd} values were plotted against distance from the fault core (Fig. 8). The resulting plot revealed that τ_{bd} values, regardless of the element investigated, tended to cluster within their above designated spatial groups, i.e., zones 1, 2, and 3 (Fig. 8). Because of this clustering affect, we overlaid τ_{wl} and their associated 95% confidence bands.

As shown in Fig. 8, regardless of spatial position, all $\tau_{bd\text{-}Si}$ values plot along or about the zero-change reference line with all sample points lying between 20% and −20% $\tau_{bd\text{-}Si}$. Additionally, $\tau_{wl\text{-}Si}$ derived from samples from zones 1 through 3 are 2% + 9%/-8%, −2% ± 2%, and −13% ± 6%, respectively (Table 5). Only the latter set of data do not include the zero-change reference line, and therefore is statistically significant (Fig. 8). Such data are consistent with no change in Si mass across zones 1 and 2, with small losses of Si mass occurring in zone 3 (Table 5).

Data derived from $\tau_{bd\text{-}K}$ calculations scatter from just below the zero-change reference line to values as high as 100% (Fig. 8). In contrast, $\tau_{wl\text{-}K}$ from zones 1 through 3 are 25% + 35%/-27%, 37% + 53%/-38%, and 14% + 66%/-42%, respectively. In Fig. 8, the 95% confidence bands for all of these data sets include the zero-change reference line and are therefore not statistically significant (Table 5).

In Fig. 8, all three sets of $\tau_{bd\text{-}Ti}$, $\tau_{bd\text{-}Mn}$, and $\tau_{bd\text{-}Fe}$ have similar distribution patterns. In these patterns, data from zones 1 and 2 scatter, plotting on, above, or below the zero-reference line, while data from

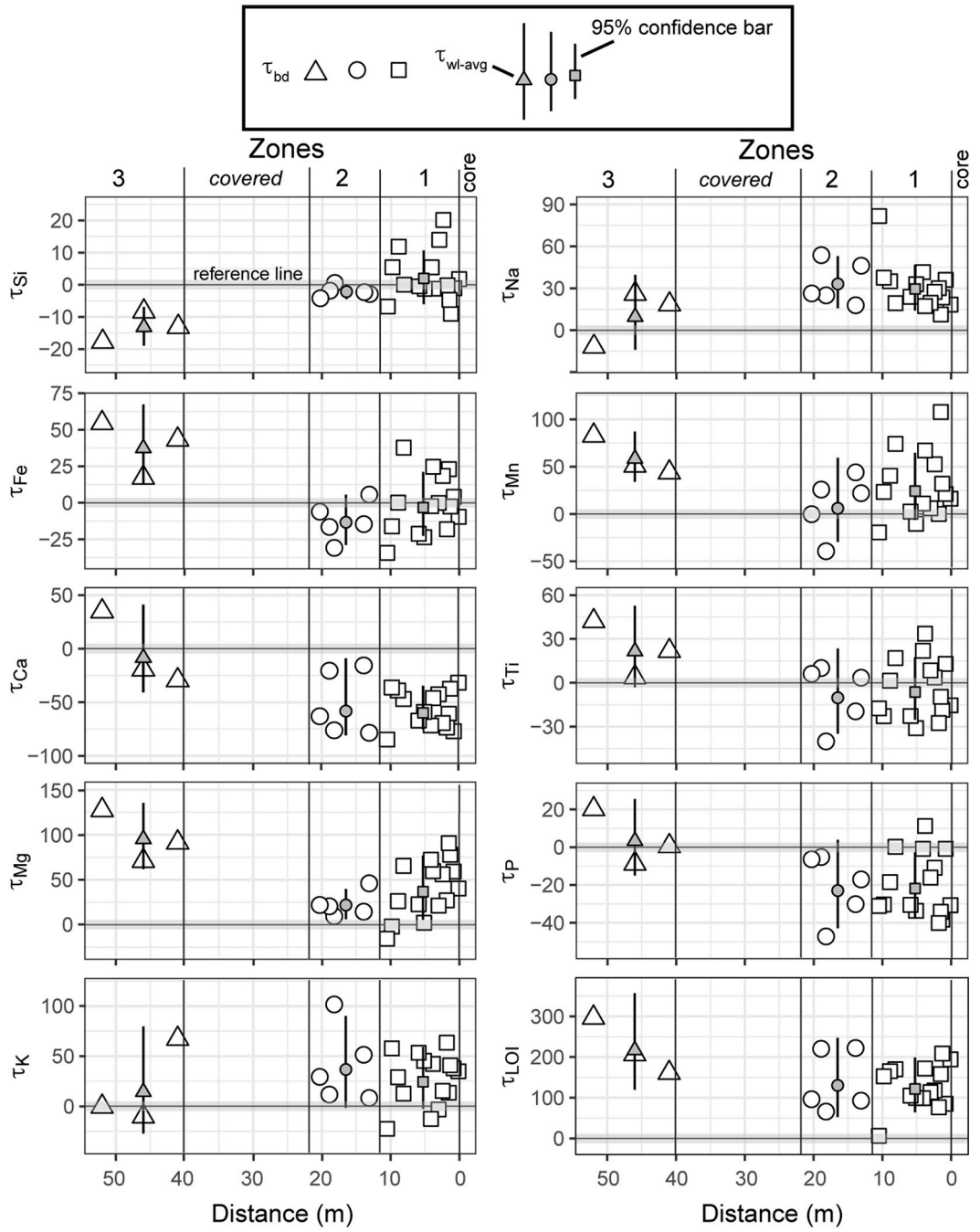

Fig. 8. Results from τ_{bd} and average τ_{wl} calculations plotted against distance from fault core. If 95% confidence band about the latter values includes zero, then result is not statistically significant. Values plotting above zero-reference signify mass gains while those falling below indicate mass losses.

zone 3 plot above. As expected, the 95% confidence bars for $\tau_{wl\text{-}Ti}$, $\tau_{wl\text{-}Mn}$, and $\tau_{wl\text{-}Fe}$ from samples analyzed from zones 1 and 2 include the zero-change reference line and are not statistically significant. In contrast, the 95% confidence bars for $\tau_{wl\text{-}Fe}$ and $\tau_{wl\text{-}Mn}$ in zone 3 do not include zero, while the opposite is true for $\tau_{wl\text{-}Ti}$. In short, Ti mass was conserved across zones 1 through 3, while Fe and Mn mass were conserved across zones 1 and 2. In contrast, Fe and Mn mass was added to zone 3.

All $\tau_{bd\text{-}Ca}$ from samples analyzed from zones 1 and 2 plot below the zero-change reference line, while samples from zone 3 plot either above or below (Fig. 8). Following in parallel, $\tau_{wl\text{-}Ca}$ are −60% + 25%/-15% for zone 1, -58% + 49%/-23% for zone 2, and -9% +50%–32% for zone 3. The latter set of data are not statistically significant, while the former are (Table 5) (Fig. 8). Such data imply that significant Ca mass was removed from zones 1 and 2 while Ca mass in zone 3 was conserved.

Samples analyzed from the zones 1 and 2 have $\tau_{bd\text{-}P}$ that scatter, plotting on, above, or below the zero-change reference line (Fig. 8). For samples from zone 1, the 95% confidence bands for $\tau_{wl\text{-}P}$ do not include 0 and are therefore statistically significant (Table 5) (Fig. 8). The opposite is true for samples analyzed from zones 2 and 3. The above data indicate that significant P mass was removed from zone 1 while P mass was statistically conserved within zones 2 and 3.

In contrast to the above data, most $\tau_{bd\text{-}Mg}$, $\tau_{bd\text{-}Na}$, *and* $\tau_{bd\text{-}LOI}$ derived from samples analyzed from zones 1 and 2 plot above the zero-reference line. In contrast, only $\tau_{bd\text{-}Mg}$ and $\tau_{bd\text{-}LOI}$ derived from samples analyzed from zone 3 follow a similar pattern, while $\tau_{bd\text{-}Na}$ plot both above and below the reference line (Fig. 8). These data suggest an increase in Mg, Na, and LOI mass in zones 1 and 2 and are supported by statistically significant $\tau_{wl\text{-}Mg}$, $\tau_{wl\text{-}Na}$, and $\tau_{wl\text{-}LOI}$ values for these areas (Table 5)

(Fig. 8). Additionally, $\tau_{wl\text{-}Mg}$ and $\tau_{wl\text{-}LOI}$ from samples analyzed from zone 3 are statistically significant, but $\tau_{wl\text{-}Na}$ is not (Fig. 8).

The above data allow some inferences to be made about the fluids that migrated through the damage zone of the Borrego fault. The losses of Ca mass within zones 1 and 2 reflect incongruent leaching from plagioclase and the sericitization of feldspars suggest an acidic character for the fluids (Brookins, 2012; Taylor and Eggleton, 2001). Such acidic conditions are also consistent with the partial dissolution of apatite. Although a small sample size, the loss of P mass within zone 1 could be caused by the dissolution of apatite. However, as P content is controlled by small amounts of apatite, primary variation in apatite content or samples that lacked the size to represent bulk apatite (P content) cannot be ruled out.

Though the oxidation state of Fe was not determined, conservation of Fe and Mn mass within zones 1 and 2 indicate interaction with an oxidizing fluid. The general increases in Mg and Na mass within these two zones likely reflect the observed chloritization of biotite and albitization of plagioclase, respectively, which require introduction of Mg^{2+} and Na^{+} (Parry and Downey, 1982; Eggleton and Banfield, 1985; Morad et al., 1990).

The statistically significant increases in Fe, Mg, and Mn in zone 3, is consistent with oxidizing conditions, and a pH less than that characteristic of the solubility field of Mn^{+2} (Brookins, 2012; Taylor and Eggleton, 2001). This latter rather loose constraint is consistent with acidic to slightly alkaline conditions (Brookins, 2012).

6. Discussion

6.1. Pre-faulting deuteric alteration in the Sierra Cucapah

Prior to development of the Borrego fault, the parent melanocratic tonalite is inferred to have undergone deuteric alteration under relatively high-temperature conditions that produced the assemblage of epidote, chlorite, titanite, and sericite. This deuteric alteration can be explained using the balanced reaction from Eggleton and Banfield (1985) if we substitute the observed secondary sericite for muscovite, as follows:

$$1\ \text{biotite} + 0.21\ \text{anorthite} + 1.64\ H_2O + 1.46H^{+} + 0.08\ O_2 \rightarrow 0.46\ \text{chlorite} + 0.11\ \text{titanite} + 0.10\ \text{epidote} + 0.56\ \text{muscovite} + 0.63\ \text{quartz} + 0.02\ \text{magnetite} + 1.46K^{+}$$

This reaction likely occurs at temperatures of ca. 330–340 °C (Eggleton and Banfield, 1985), which would have been experienced during the protracted history of post-crystallization cooling of the tonalite.

6.2. Fluid pathways and hydrothermal metasomatism in the Borrego fault zone

During development of the Borrego fault, the tonalitic parent rock was subjected to shearing and fragmentation, which led to significant grain size reduction that progressively intensifies toward the fault core producing the following sequence of fault rocks: protocataclasite, mesocataclasite, ultracataclasite. All of these fault rocks are found within the 1.5 m fault core, which also contains abundant foliated gouge and pulverized rock. The increasing density of opening-mode micro-fractures (Ostermeijer et al., 2020) likely was responsible for the observed increase in porosity toward the fault core (Fig. 7).

Taken in context, within zones 1 and 2, Mg- and Na-rich fluids are interpreted to have infiltrated the damage zone along a complex network of patchily developed interconnected fractures, producing additional chloritization of biotite and albitization of plagioclase. Similar Mg- and Na-rich brines are common among some hydrothermal systems. Truesdell et al. (1981) demonstrated in their example from the Cerro Prieto system, just ~30 km to the SE of this study area, that Mg and Na were transferred to rock while Ca was leached from rock. Additionally, Gutiérrez-Negrín (2015) documented that fluids within one sector of the Cerro Prieto system are acidic, similar to fluids along the Borrego fault. And as we have hypothesized for the Borrego fault, McLelland et al. (2002) documented albitization resulting from the infiltration of sodic brines in part of a regional hydrothermal system located in the Adirondacks, New York, USA.

Hydrothermal metasomatism, as defined by Bucher and Frey (2013) and Coombs (1961), involves hot solutions or gases percolating through fracture networks in rocks, and consequentially causing mineralogical and chemical changes in these rocks. At the study site, this stage of hydrothermal alteration involving Na- and Mg-rich fluids can be explained with the following stoichiometric reactions from Yonkee et al. (2003):

1.) $Ca_{0.17}Na_{0.83}Al_{1.17}Si_{2.83}O_8 + 0.33Na^{+} + 0.67SiO_2 \rightarrow 1.17NaAlSi_3O_8 + 0.17Ca^{2+}$
2.) $2KFe_2MgAlSi_3O_{10} + 3Mg^{2+} + 4H_2O + 3O_2 \rightarrow Mg_5Al_2Si_3O_{10}(OH)_8 + 2K^{+} + 4H^{+} + 2Fe_2O_3 + 3SiO_2$
3.) $3NaAlSi_3O_8 + K^{+} + 2H^{+} \rightarrow KAl_3Si_3O_{10}(OH)_2 + 3Na^{+} + 6SiO_2$

The alteration of oligoclase consumes Na^{+} and silica, releases Ca^{2+} and produces albite (Reaction 1). In contrast, the alteration of Fe-rich biotite consumes Mg^{2+}, releases K^{+} and H^{+}, and produces Mg-rich chlorite, silica, and oxidized Fe (Reaction 2). Acidic fluids drive the alteration of albite, which consumes K^{+}, releases Na^{+}, and produces muscovite (illite) and silica. Si is consumed by Reaction 1 but is produced by Reactions 2 and 3. In contrast, Al is conserved by all three reactions. Therefore, the three reactions operating together produce no significant additions or losses of Al and Si within the system.

While some of the Na^{+} consumed in Reaction 2 may come from the alteration of albite to muscovite (illite) (Reaction 3), the gain in Na mass in zones 1 and 2 requires an external source for Na^{+}. The above system of reactions also requires an external source for Mg^{2+} as well as a sink for Ca^{2+} and K^{+}. A possible sink for Ca^{2+} in this system is secondary calcite, as observed in thin sections of the damage zone. However, as Ca mass was generally not conserved in zones 1 and 2, we interpret that it was predominantly carried out of the system. During hydrothermal metamorphism, the movement of K^{+} produced during the formation of chlorite to sites of alteration in plagioclase may have aided formation of illite (e.g., Bétard et al., 2009), and as a result, K mass was retained within the damaged rock system (Reaction 3).

The hydrothermal brine of the Cerro Prieto geothermal field is thought to have formed from mixing Colorado River water with high salinity seawater which was then circulated to magmatic depths where it was heated and altered, adding Na and Mg to the rock while leaching Ca, K, and other elements (Truesdell et al., 1981). These changes in fluid chemistry were inferred to have been brought about by albitization, chloritization, and the formation of clays in host rock. We present strong evidence that all three processes were also operating in the Borrego fault zone, causing damaged rock to gain Na and Mg, while losing Ca mass. Being only ~30 km from the Cerro Prieto geothermal site, the source of Na- and Mg-rich fluids along the Borrego fault could be similar, although may involve meteoric-sourced waters mixing with precipitated salts of the nearby playa.

6.3. Reaction progress and cataclasis

Though we have no direct means for evaluating pressures, following Eggleton and Banfield (1985), the absence of synkinematic epidote and titanite as part of the replacement product of biotite in the damage zone samples may imply temperatures that were lower than ca. 330–340 °C. Other studies have shown that chloritization of biotite without production of epidote and titanite can occur at temperatures of ca. 200 °C (Parry and Downey, 1982). Given the apparent link between albitization and chloritization, we speculate that within zones 1 and 2 both processes

were driven by hot (~200 °C) Na- and Mg-rich fluids. Therefore, 200 °C represents an estimate of temperature for hydrothermal metasomatism driven by the infiltration of Mg- and Na-rich fluids into zones 1 and 2 of the Borrego fault zone. Although the above alteration reactions affected rocks throughout the Borrego fault zone, reaction progress depended on high porosity, dilational volumetric strain, and fracture density, and thus alteration progressed to a greater degree within zones 1 and 2 adjacent to the fault core (Figs. 6 and 7).

Although chlorite is the dominant phyllosilicate in the damaged rock system, mixed-layer clays, kaolinite, and HIV also are prevalent. These other clay species do not occur in the parent deuterically-altered tonalite, and thus their association with the damaged rock system suggest that fluids were focused through the patchily developed network of fractures within the damage zone.

Rocks in zone 3 are less fragmented than those in zones 1 and 2, but they still show an increased concentration of chlorite as well as albite alteration haloes on the rims of calcite veins. Although limited by sample size (n = 3), all analyzed samples from zone 3 show gains in Mg, and in two of the three samples an increase in Na mass is evident. It is therefore likely that rocks in zone 3 have undergone a similar hydrothermal alteration process, albeit to a much lesser degree than in zones 1 and 2. As volumetric strain and porosity approach background values in zone 3 (Fig. 7), some fractures are infilled with undamaged calcite (Fig. 3E).

6.4. Exhumation and regional geothermal

The total dip slip offset of the Borrego footwall has been estimated to be between 3 km and 4 km (Barnard, 1968), which is not sufficiently deep for the footwall to have experienced ambient temperatures of 200 °C (even using the high geothermal gradient highlighted by Espinosa-Cardeña and Campos-Enriquez (2008)) as indicated by the phase equilibria of the alteration reactions (e.g., Parry and Downey, 1982). However, additional exhumation could have taken place on the Laguna Salada fault, which is the main fault that controls the topography of the Sierra Cucapah and Laguna Salada basin and is a structure that contains the Borrego fault in its immediate footwall. To the south in Sierra El Mayor, the Laguna Salada fault is mechanically linked to the Cañada David detachment, which exposes footwall rocks that initiated at depths greater than the 200 °C isotherm (Axen et al., 2000). This relationship is supported by apatite fission track ages of 5 Ma, which are much younger than the onset of faulting, and by modeling of Ar diffusion in K-feldspar, which has a blocking temperature of 220 °C (Axen et al., 2000). There is likely a northward decreasing gradient in unroofing through the Sierra Cucapah (Axen and Fletcher, 1998), and thus prior to the onset of faulting, the rocks of our study area along the Borrego fault likely resided at higher levels in the crust with cooler ambient temperatures. Nonetheless, phase equilibria suggest that temperatures in the fault zone reached 200 °C, which suggests that the fault zone has experienced hotter temperatures than the surrounding rocks, perhaps due to the channeling of hydrothermal fluids along the Borrego fault zone.

Regional heat flow is high (>100 mW/m^2) in northern Baja California (Lachenbruch et al., 1985) and local heat flow in and around Laguna Salada basin is even higher (>200 mW/m^2) (Chavez et al., 2000; Prol-Ledesma and Morán-Zenteno, 2019). Currently, a high geothermal gradient in the region is well documented by the presence of the Cerro Prieto geothermal field (Nehring and D'Amore, 1984), the fumarole generated along the 2010 rupture of the nearby Pescadores fault (Fletcher et al., 2014), extensive deposits of silica and native sulfur associated with the Cañada David detachment, and reports of high surface temperatures observed in field studies by some of the authors of this paper and Barnard (1968). In one such example, Rockwell observed temperatures of ~70 °C at 1 m depth in a soil pit dug into fan 3 (Mueller and Rockwell, 1995) along the Laguna Salada fault. Other soil pits along the Laguna Salada fault in the area of high temperatures exposed petrosalic horizons, which suggests that the hydrothermal solutions are probably brine-like in character. In addition, along the Laguna Salada fault, near the study area at the latitude of 32.44°N, there is a hot spring that currently expels salty solutions and forms a pool on the basin floor (Chavez et al., 2000). Because the Borrego and Laguna Salada faults are connected by a more shallowly inclined fault at depth (Fletcher et al., 2016), both should act as conduits for geothermal systems at depth.

6.5. Alteration and deformation history

In summation, a parent tonalite experiences the following sequence of alteration and deformation to obtain its current mineralogical and geochemical character:

1.) The parent tonalite pluton underwent pervasive deuteric alteration, leading to a chlorite-epidote-titanite-sericite assemblage.
2.) The deuterically-altered parent tonalite was fractured and fragmented in the footwall of the Borrego fault zone. Within a complex patchily developed network of fractures (Ostermeijer et al., 2020), interconnectivity of porosity was increased.
3.) The enhanced permeability of the Borrego fault zone allowed the percolation of hydrothermal fluids, rich in Mg and Na, through zones 1 and 2, and to a lesser extent zone 3. The infiltrating fluids drove albitization and chloritization. Hydrothermal alteration through brine solution deposition is well-developed along both the Borrego and Laguna Salada faults. Thus, alteration that would normally be associated with higher temperatures and deeper levels of exhumation are present at the surface in the rising fault block between these two Plio-Quaternary faults (Fig. 9).

6.6. Implications for fault zone strength

The alterations that have occurred in the Borrego fault zone may influence mechanical properties of the fault rocks. The development of phyllosilicates, including chlorite, sericite, and clay minerals, introduces mechanical anisotropies into the rock mass. Specifically, platy phyllosilicates with a preferred orientation in gouge or subsidiary shears lead to an anisotropic permeability structure (Morrow et al., 1984; Evans et al., 1997; Zhang et al., 1999). In such cases, fluid flow can be focused along the fault or other clay-bearing shears elevating pore pressure along that plane. Increasing pore pressure results in a decrease in effective normal stress on a plane and makes slip along such a plane more favorable (Sibson, 1990; Rice, 1992). Compartmentalization of fluid flow along faults throughout the Sierra Cucapah may be attributed to the development of phyllosilicate-rich alteration products. Phyllosilicates can also have a weakening effect on faults due to their strength anisotropy. When preferentially aligned, phyllosilicate minerals have low coefficients of friction (Moore and Laukner, 2004) and fault zones rich in phyllosilicates are frictionally weaker than other fault zones (Wintsch et al., 1995; Tesei et al., 2012) leading to an overall lower resistance to slip.

The Borrego fault zone is rich in phyllosilicates and may therefore be relatively weak compared to unaltered host rock, but other factors relating to deformation may counter these weakening processes. Fractures in the damage zone have been sealed by calcite leading to reduced microfracture porosity, a process that may have a strengthening effect as observed in other natural fault zones (e.g., Callahan et al., 2019). The competing weakening and strengthening effects of alteration and sealing of fractures may lead to a strength disparity between weak phyllosilicate-rich shears and stronger rock that contains sealed microfractures in the damage zone. Sealing of microfractures is strongly rate-dependent, but under favorable precipitation environments, we expect strain to localize to the weaker clay-rich shear bands. In unfavorable precipitation conditions, unfilled microfractures remain weak and are more favorable to accommodate slip, leading to generally more distributed deformation. Fletcher et al. (2020) found that parts of the Borrego fault experienced highly localized deformation during the 2010

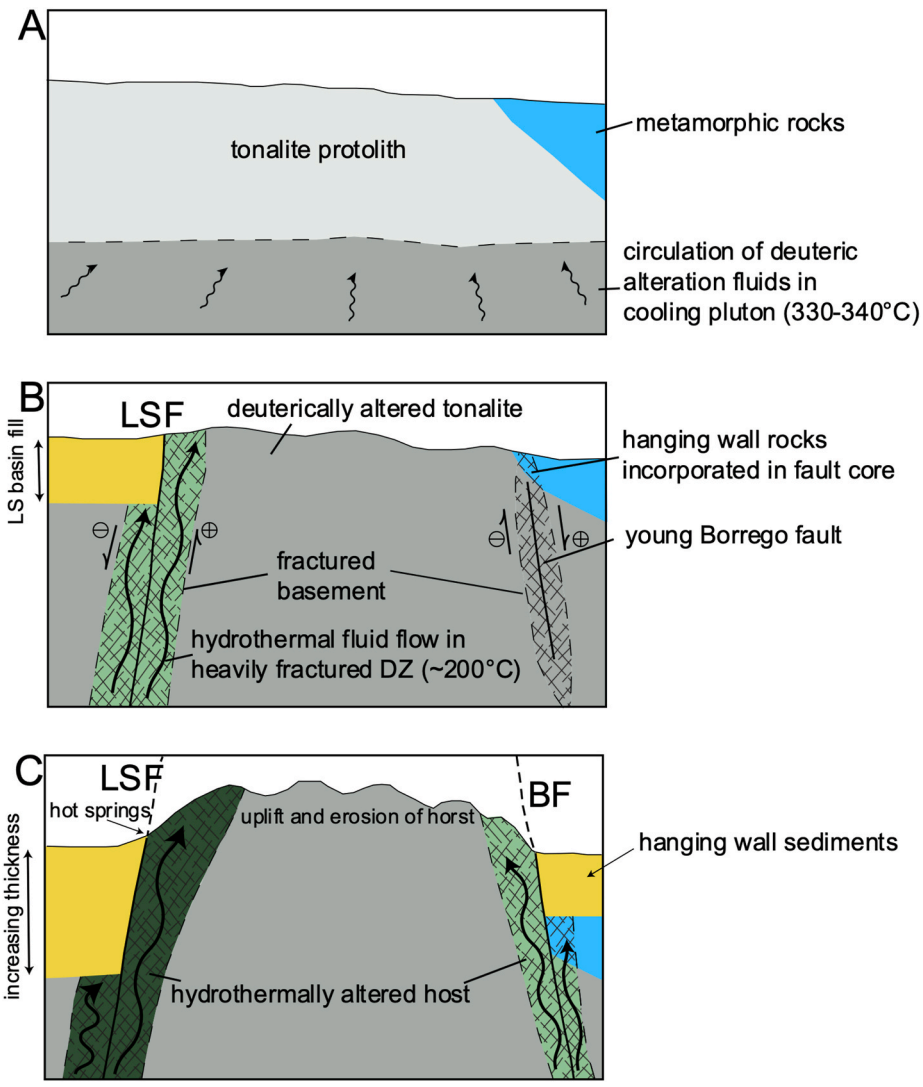

Fig. 9. Schematic sequential cross-section of horst block between Borrego fault (BF) and Laguna Salada fault (LSF). (A) Intrusion and cooling of granitoid plutons ~95 Ma. Deuteric alteration occurred at temperatures of 330–340 °C. (B) Onset of faulting in deuterically-altered host rock and uplift of horst block ~10 Ma. Increase in fracture density produces an increase in permeability. (C) Active faulting in the Sierra Cucapah. Permeable fault zone rocks provide conduit for hydrothermal fluids (~200 °C) which further alter the host rock. Continued uplift and erosion of horst block through 0 Ma.

EMC earthquake, while other sections displayed more distributed deformation across a wider zone. Thus, localization of slip on the Borrego fault may vary from event to event. A cycle of fracturing, alteration, and reduction of microfracture porosity is likely heterogeneous in both rate and spatial distribution, thus plausibly contributing to the sectioning of the degree of localization from one event to the next.

7. Conclusions

Detailed fault zone studies, such as this one, provide valuable insight into processes operating in fault damage zones at outcrop scale. Our field and microscopic data demonstrate that deformation and hydrothermal alteration of a deuterically-modified tonalitic protolith increases toward the fault core as a result of increased porosity from fracturing. Elemental mass redistribution in the fault damage zone is likely driven by increased permeability and reactive surface area from fracturing which controls fluid-rock interactions. The primary driving forces in the geochemical alteration of the horst tonalitic block seem to be albitization and chloritization caused by infiltration of Mg- and Na-rich oxidizing fluids. These processes appear to have increased in intensity towards the fault core along the highly fractured fault damage zone of the Borrego fault studied in this investigation.

CRediT author statement

Matthew T. Dorsey: Conceptualization, Validation, Formal analysis, Investigation, Data curation, Writing – Original Draft, Writing – Review & Editing, Visualization, Project administration, Funding acquisition.

Thomas K. Rockwell: Conceptualization, Writing – Review & Editing, Supervision, Funding acquisition.

Gary H. Girty: Conceptualization, Methodology, Software, Formal analysis, Resources, Data curation, Writing – Review & Editing, Visualization, Supervision.

Giles A. Ostermeijer: Writing – Review & Editing, Visualization.

John Browning: Writing – Review & Editing.

Thomas M. Mitchell: Conceptualization, Writing – Review & Editing.

John M. Fletcher: Writing – Review & Editing.

Declaration of competing interest

The authors declare that they have no known competing financial interests or personal relationships that could have appeared to influence the work reported in this paper.

Acknowledgements

This research was supported by the Southern California Earthquake Center (Contribution #10037). SCEC is funded by NSF Cooperative Agreement EAR-1600087 & USGS Cooperative Agreement G17AC00047. Additional funding, awarded to MTD, was provided by the AEG Foundation and AAPG Foundation Grants-in-Aid Program. Many thanks are extended to S. Laubach, A. Berger, and an anonymous reviewer for their perspicacious suggestions that have greatly improved the quality of this paper. Invaluable lab support was provided by H. Webb and J. Kimbrough at SDSU. Lastly, we acknowledge colleagues from SDSU and CICESE who were instrumental in completing fieldwork.

Appendix A. Supplementary data

Supplementary data to this article can be found online at https://doi.org/10.1016/j.jsg.2020.104269.

References

Ague, J.J., 1994. Mass transfer during Barrovian metamorphism of pelites, south-central Connecticut; I, Evidence for changes in composition and volume. Am. J. Sci. 294, 989–1057.

Aitchison, J., 1982. The statistical analysis of compositional data. J. Roy. Stat. Soc. B (Methodol.) 44, 139–160. https://doi.org/10.1111/j.2517-6161.1982.tb01195.x.

Aitchison, J., 1986. The Statistical Analysis of Compositional Data. Chapman and Hall.

Aitchison, J., 1989. Measures of location of compositional data sets. Math. Geol. 21, 787–790. https://doi.org/10.1007/BF00893322.

Axen, G.J., Fletcher, J.M., 1998. Late Miocene-Pleistocene extensional faulting, northern Gulf of California, Mexico and Salton Trough, California. Int. Geol. Rev. 40, 217–244.

Axen, G.J., Grove, M., Stockli, D., Lovera, O.M., Rothstein, D.A., Fletcher, J.M., Farley, K., Abbott, P.L., 2000. Thermal evolution of Monte Blanco dome: low-angle normal faulting during Gulf of California rifting and late Eocene denudation of the eastern Peninsular Ranges. Tectonics 19, 197–212.

Bailey, E.H., 1960. Selective staining of K-feldspar and plagioclase on rock slab and thin sections. Am. Mineral. 45, 1020–1025.

Barnard, F.L., 1968. Structural geology of the Sierra de los Cucapas, northeastern Baja California, Mexico, and Imperial County, California. University of Colorado, Boulder, CO, USA.

Barton, C.A., Zoback, M.D., Moos, D., 1995. Fluid flow along potentially active faults in crystalline rock. Geology 23, 683–686, 10.1130/0091-7613(1995)023<0683:Ffapaf>2.3.Co;2.

Bétard, F., Caner, L., Gunnell, Y., Bourgeon, G., 2009. Illite neoformation in plagioclase during weathering: evidence from semi-arid Northeast Brazil. Geoderma 152, 53–62.

Brimhall, G.H., Dietrich, W.E., 1987. Constitutive mass balance relations between chemical composition, volume, density, porosity, and strain in metasomatic hydrochemical systems: results on weathering and pedogenesis. Geochem. Cosmochim. Acta 51, 567–587.

Brookins, D.G., 2012. Eh-pH Diagrams for Geochemistry. Springer Science & Business Media.

Brown, S.R., Bruhn, R.L., 1998. Fluid permeability of deformable fracture networks. J. Geophys. Res. Solid Earth 103, 2489–2500. https://doi.org/10.1029/97jb03113.

Bruhn, R.L., Yonkee, W.A., Parry, W.T., 1990. Structural and fluid-chemical properties of seismogenic normal faults. Tectonophysics 175, 139–157. https://doi.org/10.1016/0040-1951(90)90135-U.

Bruhn, R.L., Parry, W.T., Yonkee, W.A., Thompson, T., 1994. Fracturing and hydrothermal alteration in normal fault zones. Pure Appl. Geophys. 142, 609–644. https://doi.org/10.1007/BF00876057.

Bucher, K., Frey, M., 2013. Petrogenesis of Metamorphic Rocks. Springer Berlin Heidelberg.

Caine, J.S., Evans, J.P., Forster, C.B., 1996. Fault zone architecture and permeability structure. Geology 24, 1025–1028.

Callahan, O.A., Eichhubl, P., Olson, J.E., Davatzes, N.C., 2019. Fracture mechanical properties of damaged and hydrothermally altered rocks, Dixie Valley-stillwater fault zone, Nevada, USA. J. Geophys. Res. Solid Earth 124, 4069–4090. https://doi.org/10.1029/2018JB016708.

Carrasco, T., Girty, G., 2015. Identifying a reference frame for calculating mass change during weathering: a review and case study utilizing the C# program assessing element immobility and critical ratio methodology. Catena 125, 146–161.

Chavez, R.E., Flores, E.L., Campos, J.O., Ladron De Guevara, M., Fernandez-Puga, M.C., Herrera, J., 2000. Three-dimensional structure of the Laguna Salada basin and its thermal regime. Geophys. Prospect. 48, 835–870. https://doi.org/10.1046/j.1365-2478.2000.00215.x.

Clinkenbeard, J.P., 1987. The Mineralogy, Geochemistry, and Geochronology of the La Posta Pluton, San Diego and Imperial Counties, California. San Diego State University, San Diego, CA, USA.

Clinkenbeard, J.P., Walawender, M.J., 1989. Mineralogy of the La Posta pluton: implications for the origin of zoned plutons in the eastern peninsular ranges batholith, southern and Baja California. Am. Mineral. 74, 1258–1269.

Coombs, D., 1961. Some recent work on the lower grades of metamorphism. Aust. J. Sci. 24, 203–215.

Curewitz, D., Karson, J.A., 1997. Structural settings of hydrothermal outflow: fracture permeability maintained by fault propagation and interaction. J. Volcanol. Geoth. Res. 79, 149–168. https://doi.org/10.1016/S0377-0273(97)00027-9.

Denny, A.C., Fall, A., Orland, I.J., Valley, J.W., Eichhubl, P., Laubach, S.E., 2019. A history of pore water oxygen isotope evolution in the Cretaceous Travis Peak Formation in East Texas. Geol. Soc. Am. Bull. 132, 1626–1638. https://doi.org/10.1130/b35291.1.

Dibblee Jr., T.W., 1954. Geology of the Imperial valley region, California. Geol. South. Calif. Calif. Div. Mine. Bull. 170, 21–28.

Dorsey, M.T., Rockwell, T.K., Girty, G.H., Ostermeijer, G.A., Mitchell, T.M., Fletcher, J. M., 2017. Evidence of Na- and Mg-Rich Hydrothermal Brines Driving Chloritization and Albitization in an Active Fault Zone: Case Study of the Borrego Fault, Baja CA, Mexico. Southern California Earthquake Center Annual Meeting, Palm Springs, CA, USA.

Eggleton, R.A., Banfield, J.F., 1985. The alteration of granitic biotite to chlorite. Am. Mineral. 70, 902–910.

Espinosa-Cardeña, J.M., Campos-Enriquez, J.O., 2008. Curie point depth from spectral analysis of aeromagnetic data from Cerro Prieto geothermal area, Baja California, México. J. Volcanol. Geoth. Res. 176, 601–609. https://doi.org/10.1016/j.jvolgeores.2008.04.014.

Evans, J.P., Chester, F.M., 1995. Fluid-rock interaction in faults of the San Andreas system: inferences from San Gabriel fault rock geochemistry and microstructures. J. Geophys. Res. Solid Earth 100, 13007–13020.

Evans, J.P., Forster, C.B., Goddard, J.V., 1997. Permeability of fault-related rocks, and implications for hydraulic structure of fault zones. J. Struct. Geol. 19, 1393–1404. https://doi.org/10.1016/S0191-8141(97)00057-6.

Færseth, R.B., 2006. Shale smear along large faults: continuity of smear and the fault seal capacity. J. Geol. Soc. 163, 741–751. https://doi.org/10.1144/0016-76492005-162.

Fletcher, J.M., Grove, M., Kimbrough, D., Lovera, O., Gehrels, G.E., 2007. Ridge-trench interactions and the Neogene tectonic evolution of the Magdalena shelf and southern Gulf of California: insights from detrital zircon U-Pb ages from the Magdalena fan and adjacent areas. Geol. Soc. Am. Bull. 119, 1313–1336. https://doi.org/10.1130/b26067.1.

Fletcher, J.M., Oskin, M.E., Teran, O.J., 2016. The role of a keystone fault in triggering the complex El Mayor–Cucapah earthquake rupture. Nat. Geosci. 9, 303–307. https://doi.org/10.1038/ngeo2660.

Fletcher, J.M., Teran, O.J., Rockwell, T.K., Oskin, M.E., Hudnut, K.W., Mueller, K.J., Spelz, R.M., Akciz, S.O., Masana, E., Faneros, G., 2014. Assembly of a large earthquake from a complex fault system: surface rupture kinematics of the 4 April 2010 El Mayor–Cucapah (Mexico) Mw 7.2 earthquake. Geosphere 10, 797–827.

Fletcher, J.M., Teran, O.J., Rockwell, T.K., Oskin, M.E., Hudnut, K.W., Spelz, R.M., Lacan, P., Dorsey, M.T., Ostermeijer, G., Mitchell, T.M., Akciz, S.O., Hernandez-Flores, A.P., Hinojosa-Corona, A., Peña-Villa, I., Lynch, D.K., 2020. An analysis of the factors that control fault zone architecture and the importance of fault orientation relative to regional stress. Geol. Soc. Am. Bull. https://doi.org/10.1130/b35308.1.

García-Abdeslem, J., Espinosa-Cardeña, J., Munguía-Orozco, L., Wong-Ortega, V., Ramirez- Hernández, J., 2001. Crustal structure from 2-D gravity and magnetics modeling, and seismotectonics in the Laguna Salada Basin, northern Baja California, México. Geofisc. Int. 40, 67–85.

Girty, G.H., Biggs, M.A., Berry, R.W., 2008. An unusual occurrence of probable Pleistocene corestone within a Cretaceous dioritic enclave, Peninsular Ranges, California. Catena 74 (1), 43–57. https://doi.org/10.1016/j.catena.2008.03.009.

Girty, G.H., Stephenson, D., Canfield, A., Marsh, J., Middleton, T., Rayburn, J., Sisk, M., Verdugo, D., Moniz, R., Gunter, J., 2006. Geology of Picacho State Recreation Area, SE California: Implications for the Timing of the Formation of the Chocolate Mountains Anticlinorium. Using Stratigraphy, Sedimentology, and Geochemistry to Unravel the Geologic History of the Southwestern Cordillera: A Volume in Honor of Patrick L. Abbott. Pacific Section SEPM.

Gutiérrez-Negrín, L., 2015. Mexican geothermal plays, Proceedings of the world geothermal congress 2015. Melbourne, Australia, 19–25 April.

Goddard, J.V., Evans, J.P., 1995. Chemical changes and fluid-rock interaction in faults of crystalline thrust sheets, northwestern Wyoming, U.S.A. J. Struct. Geol. 17, 533–547. https://doi.org/10.1016/0191-8141(94)00068-B.

Gudmundsson, A., 2000. Active fault zones and groundwater flow. Geophys. Res. Lett. 27 (18), 2993–2996. https://doi.org/10.1029/1999gl011266.

Hagemann, S.G., Neumayr, P., Yardley, B.W.D., Banks, D.A., Couture, J.-F., Landis, G.P., Rye, R., 2007. Fluid chemistry and evolution of hydrothermal fluids in an Archaean transcrustal fault zone network: the case of the Cadillac Tectonic Zone, Abitibi greenstone belt, Canada. Can. J. Earth Sci. 44, 745–773. https://doi.org/10.1139/e06-130.

Harris, W.G., Hollien, K.A., Bates, S.R., Acree, W.A., 1992. Dehydration of hydroxy-interlayered vermiculite as a function of time and temperature. Clay Clay Miner. 40, 335–340. https://doi.org/10.1346/CCMN.1992.0400314.

Hernandez Flores, A.P., 2015. Paleosismología del sistema de fallas imbricado en la Sierra Cucapah, Baja California. Centro de Investigación Científica y de Educación Superior de Ensenada, México.

Hernandez Flores, A.P., Fletcher, J.M., Spelz, R., Rockwell, T.K., Teran, O.J., 2013. Paleoseismology of the imbricate fault array in the Sierra Cucapah, Northern Baja California, Mexico. In: American Geophysical Union Meeting of the Americas, Cancun, Mexico.

Hickman, S., Sibson, R., Bruhn, R., 1995. Introduction to special section: mechanical involvement of fluids in faulting. J. Geophys. Res. Solid Earth 100 (B7), 12831–12840. https://doi.org/10.1029/95jb01121.

Hileman, J.A., Allen, C.R., Nordquist, J.M., 1973. Seismicity of the Southern California Region: 1 Jan. 1932 to 31 Dec. 1972. Seismological Laboratory, California Institute of Technology, Pasadena, CA, USA.

Ishikawa, T., Tanimizu, M., Nagaishi, K., Matsuoka, J., Tadai, O., Sakaguchi, M., Hirono, T., Mishima, T., Tanikawa, W., Lin, W., Kikuta, H., Soh, W., Song, S.-R., 2008. Coseismic fluid–rock interactions at high temperatures in the Chelungpu fault. Nat. Geosci. 1, 679–683. https://doi.org/10.1038/ngeo308.

Kelm, D.L., 1972. A Gravity and Magnetic Study of the Laguna Salada Area, Baja California, Mexico. San Diego State University, San Diego, CA, USA.

Kerr, P.F., 1959. Optical Mineralogy.

Kerrich, R., 1986. Fluid infiltration into fault zones: chemical, isotopic, and mechanical effects. Pure Appl. Geophys. 124, 225–268. https://doi.org/10.1007/bf00875727.

Lachenbruch, A.H., Sass, J.H., Galanis, S.P., 1985. Heat flow in southernmost California and the origin of the Salton Trough. J. Geophys. Res. Atmos. 90, 6709–6736. https://doi.org/10.1029/jb090ib08p06709.

Laubach, S.E., Lander, R.H., Criscenti, L.J., Anovitz, L.M., Urai, J.L., Pollyea, R.M., Hooker, J.N., Narr, W., Evans, M.A., Kerisit, S.N., Olson, J.E., Dewers, T., Fisher, D., Bodnar, R., Evans, B., Dove, P., Bonnell, L.M., Marder, M.P., Pyrak-Nolte, L., 2019. The role of chemistry in fracture pattern development and opportunities to advance interpretations of geological materials. Rev. Geophys. 57, 1065–1111. https://doi.org/10.1029/2019RG000671.

Le Maitre, R.W., Streckeisen, A., Zanettin, B., Le Bas, M., Bonin, B., Bateman, P., 2005. Igneous Rocks: a Classification and Glossary of Terms: Recommendations of the International Union of Geological Sciences Subcommission on the Systematics of Igneous Rocks. Cambridge University Press.

Mammerickx, J., Klitgord, K.D., 1982. Northern east Pacific rise - evolution from 25 MYBP to the present. J. Geophys. Res. 87, 6751–6759. https://doi.org/10.1029/JB087iB08p06751.

McLelland, J., Morrison, J., Selleck, B., Cunningham, B., Olson, C., Schmidt, K., 2002. Hydrothermal alteration of late-to post-tectonic Lyon Mountain Granitic Gneiss, Adirondack Mountains, New York: origin of quartz–sillimanite segregations, quartz–albite lithologies, and associated Kiruna-type low-Ti Fe-oxide deposits. J. Metamorph. Geol. 20, 175–190.

Mendenhall, W., Beaver, R.J., 1994. Introduction to Probability and Statistics, ninth ed. Duxbury Press.

Miller, W.J., 1935. Geologic section across the southern peninsular range of California: Calif. J. Mine. Geol. State Mineral. Rep. 31, 115–142.

Mitchell, T.M., Faulkner, D.R., 2009. The nature and origin of off-fault damage surrounding strike-slip fault zones with a wide range of displacements: a field study from the Atacama fault system, northern Chile. J. Struct. Geol. 31, 802–816. https://doi.org/10.1016/j.jsg.2009.05.002.

Moniz, R., 2008. Geochemistry and U/Pb Geochronology of the Eastern-Most Peninsular Ranges Batholith of Southern California and Northern Baja California, Geological Sciences. San Diego State University, San Diego, CA, USA.

Moore, D.E., Lockner, D.A., 2004. Crystallographic controls on the frictional behavior of dry and water-saturated sheet structure minerals. J. Geophys. Res. Solid Earth 109. https://doi.org/10.1029/2003JB002582.

Moore, D.M., Reynolds, R.C., 1989. X-ray Diffraction and the Identification and Analysis of Clay Minerals. Oxford university press, Oxford.

Morad, S., Bergan, M., Knarud, R., Nystuen, J.P., 1990. Albitization of detrital plagioclase in Triassic reservoir sandstones from the Snorre field, Norwegian North sea. J. Sediment. Res. 60.

Morrow, C.A., Shi, L.Q., Byerlee, J.D., 1984. Permeability of fault gouge under confining pressure and shear stress. J. Geophys. Res. Solid Earth 89, 3193–3200. https://doi.org/10.1029/JB089iB05p03193.

Morton, N., Girty, G.H., Rockwell, T.K., 2012. Fault zone architecture of the San Jacinto fault zone in Horse Canyon, southern California: a model for focused post-seismic fluid flow and heat transfer in the shallow crust. Earth Planet. Sci. Lett. 329–330, 71–83. https://doi.org/10.1016/j.epsl.2012.02.013.

Mueller, K.J., Rockwell, T., 1991. Late Quaternary Structural Evolution of the Western Margin of the Sierra Cucapa, Northern Baja California. The Gulf and Peninsular Province of the Californians, vol. 47. American Association of Petroleum Geologists Memoir, pp. 249–260.

Mueller, K.J., Rockwell, T.K., 1995. Late quaternary activity of the Laguna Salada fault in northern Baja California, Mexico. Geol. Soc. Am. Bull. 107, 8–18.

Nehring, N.L., D'Amore, F., 1984. Gas chemistry and thermometry of the Cerro Prieto, Mexico, geothermal field. Geothermics 13, 75–89. https://doi.org/10.1016/0375-6505(84)90008-7.

Ostermeijer, G.A., Mitchell, T.M., Aben, F.M., Dorsey, M.T., Browning, J., Rockwell, T.K., Fletcher, J.M., Ostermeijer, F., 2020. Damage zone heterogeneity on seismogenic faults in crystalline rock; a field study of the Borrego Fault, Baja California. J. Struct. Geol. 104016. https://doi.org/10.1016/j.jsg.2020.104016.

Parry, W., Downey, L., 1982. Geochemistry of hydrothermal chlorite replacing igneous biotite. Clay Clay Miner. 30, 81–90.

Parry, W.T., Hedderly-Smith, D., Bruhn, R.L., 1991. Fluid inclusions and hydrothermal alteration on the Dixie valley fault, Nevada. J. Geophys. Res. Solid Earth 96, 19733–19748. https://doi.org/10.1029/91JB01965.

Parry, W.T., 1998. Fault-fluid compositions from fluid-inclusion observations and solubilities of fracture-sealing minerals. Tectonophysics 290, 1–26. https://doi.org/10.1016/S0040-1951(98)00013-4.

Pawlowsky-Glahn, V., Egozcue, J.J., 2006. Compositional data and their analysis: an introduction. Geol. Soc. Lond. Spec. Publ. 264, 1–10. https://doi.org/10.1144/gsl.Sp.2006.264.01.01.

Prol-Ledesma, R.M., Morán-Zenteno, D.J., 2019. Heat flow and geothermal provinces in Mexico. Geothermics 78, 183–200. https://doi.org/10.1016/j.geothermics.2018.12.009.

Purcell, J.W., Lovelace, F.D., Girty, G.H., 2015. Biotite controlled chemical alteration of granodioritic–tonalitic saprock: exploring the use of sieving to enhance compositional linear trends. Geoderma 253, 90–101.

Rempe, M., Mitchell, T., Renner, J., Nippress, S., Ben-Zion, Y., Rockwell, T., 2013. Damage and seismic velocity structure of pulverized rocks near the San Andreas Fault. J. Geophys. Res. Solid Earth 118, 2813–2831. https://doi.org/10.1002/jgrb.50184.

Rice, J.R., 1992. Chapter 20 fault stress states, pore pressure distributions, and the weakness of the san Andreas fault. In: Evans, B., Wong, T.-f. (Eds.), International Geophysics, vol. 51, pp. 475–503. https://doi.org/10.1016/S0074-6142(08)62835-1.

Righi, D., Petit, S., Bouchet, A., 1993. Characterization of hydroxy-interlayered vermiculite and illite/smectite interstratified minerals from the weathering of chlorite in a cryorthod. Clay Clay Miner. 41, 484–495. https://doi.org/10.1346/CCMN.1993.0410409.

Rockwell, T., Sisk, M., Girty, G., Dor, O., Wechsler, N., Ben-Zion, Y., 2009. Chemical and physical characteristics of pulverized Tejon lookout granite adjacent to the san Andreas and Garlock faults: implications for earthquake physics. Pure Appl. Geophys. 166, 1725–1746. https://doi.org/10.1007/s00024-009-0514-1.

Rockwell, T.K., Hernandez, A.P., Fletcher, J.M., Teran, O.J., Mueller, K.J., Salisbury, J.B., Akciz, S.O., Štěpančíková, P., 2015. Reassessment of the 1892 Laguna Salada earthquake: fault kinematics and rupture patterns. Bull. Seismol. Soc. Am. 105, 2885–2893. https://doi.org/10.1785/0120140274.

Rossetti, F., Aldega, L., Tecce, F., Balsamo, F., Billi, A., Brilli, M., 2010. Fluid flow within the damage zone of the Boccheggiano extensional fault (Larderello–Travale geothermal field, central Italy): structures, alteration and implications for hydrothermal mineralization in extensional settings. Geol. Mag. 148, 558–579. https://doi.org/10.1017/s001675681000097x.

Seiler, C., Gleadow, A.J.W., Fletcher, J.M., Kohn, B.P., 2009. Thermal evolution of a sheared continental margin: insights from the Ballenas transform in Baja California, Mexico. Earth Planet. Sci. Lett. 285, 61–74. https://doi.org/10.1016/j.epsl.2009.05.043.

Sheldon, H.A., Micklethwaite, S., 2007. Damage and permeability around faults: implications for mineralization. Geology 35, 903–906. https://doi.org/10.1130/g23860a.1.

Sibson, R.H., 1990. Conditions for fault-valve behaviour. Geol. Soc. Lond. Spec. Publ. 54 (1), 15–28. https://doi.org/10.1144/gsl.Sp.1990.054.01.02.

Sibson, R.H., 1996. Structural permeability of fluid-driven fault-fracture meshes. J. Struct. Geol. 18, 1031–1042. https://doi.org/10.1016/0191-8141(96)00032-6.

Stierman, D.J., 1984. Geophysical and geological evidence for fracturing, water circulation and chemical alteration in granitic rocks adjacent to major strike-slip faults. J. Geophys. Res. Solid Earth 89, 5849–5857. https://doi.org/10.1029/JB089iB07p05849.

Strand, C.L., 1980. Pre-1900 Earthquakes of Baja California and San Diego County. San Diego State University, San Diego, CA, USA.

Taylor, G., Eggleton, R.A., 2001. Regolith Geology and Geomorphology. John Wiley & Sons.

Team, R.C., 2015. R: A Language and Environment for Statistical Computing. R Foundation for Statistical Computing, Vienna, Austria.

Tesei, T., Collettini, C., Carpenter, B.M., Viti, C., Marone, C., 2012. Frictional strength and healing behavior of phyllosilicate-rich faults. J. Geophys. Res. Solid Earth 117. https://doi.org/10.1029/2012JB009204.

Truesdell, A., Thompson, J., Coplen, T., Nehring, N., Janik, C., 1981. The origin of the Cerro Prieto geothermal brine. Geothermics 10, 225–238.

Tulloch, A.J., Kimbrough, D.L., 2003. Paired Plutonic Belts in Convergent Margins and the Development of High Sr/Y Magmatism: peninsular Ranges Batholith of Baja-California and Median Batholith of New Zealand. Special paper-Geological Society of America, pp. 275–295.

Walawender, M., Gastil, R., Clinkenbeard, J., McCormick, W., Eastman, B., Wernicke, R., Wardlaw, M., Gunn, S., Smith, B., 1990. Origin and evolution of the zoned La Posta-type plutons, eastern Peninsular Ranges batholith, southern and Baja California. Geol. Soc. Am. Mem. 174, 1–18.

Warren, H.N., Girty, G.H., 1999. A matlab 5 program for calculating the statistics of mass change. J. Geosci. Educ. 47, 313–320. https://doi.org/10.5408/1089-9995-47.4.313.

Wintsch, R.P., Christoffersen, R., Kronenberg, A.K., 1995. Fluid-rock reaction weakening of fault zones. J. Geophys. Res. Solid Earth 100, 13021–13032. https://doi.org/10.1029/94JB02622.

Woodcock, N., Mort, K., 2008. Classification of fault breccias and related fault rocks. Geol. Mag. 145, 435–440.

Woronow, A., Love, K.M., 1990. Quantifying and testing differences among means of compositional data suites. Math. Geol. 22, 837–852.

Yonkee, W.A., Parry, W.T., Bruhn, R.L., 2003. Relations between progressive deformation and fluid-rock interaction during shear-zone growth in a basement-cored thrust sheet, Sevier orogenic belt, Utah. Am. J. Sci. 303, 1–59. https://doi.org/10.2475/ajs.303.1.1.

Zhang, S., Tullis, T.E., Scruggs, V.J., 1999. Permeability anisotropy and pressure dependency of permeability in experimentally sheared gouge materials. J. Struct. Geol. 21, 795–806. https://doi.org/10.1016/S0191-8141(99)00080-2.

Zhang, X., Sanderson, D.J., 1996. Numerical modelling of the effects of fault slip on fluid flow around extensional faults. J. Struct. Geol. 18, 109–119. https://doi.org/10.1016/0191-8141(95)00086-S.